An Initial Orbit Determination Method Using Single-Site Very Short Arc Radar Observations

SHUO ZHANG
TUO FU
DEFENG CHEN
SHUAI DING
MEIGUO GAO
Beijing Institute of Technology, Beijing, China

A new initial orbit determination (IOD) method using single-site very short arc radar observations is proposed. The method uses slant range, azimuth, and elevation angles to determine the position vector and uses higher order radial measurements (velocity, acceleration, and jerk) to determine the velocity vector. The IOD accuracy based on the geometric dilution of precision (GDOP) metric is analyzed using a linearization approach. Relations between the GDOP and the observation geometry are investigated under a near-circular constraint and the optimal observation geometry for determining the velocity vector is identified. Monte Carlo simulations are presented for a typical low-Earth orbit satellite under two observation geometry configurations. The results demonstrate that the proposed method is feasible for very short arc initial orbit determination.

Authors' address: S. Zhang, T. Fu, D. Chen, S. Ding and M. Gao are with the School of Information and Electronics, Beijing Institute of Technology, Beijing 100081, China, E-mail: (zsmathbit@gmail.com; futuobit@gmail.com; defengchenbit@gmail.com; dingsabc@gmail.com; meiguo_g@bit.edu.cn). *(Corresponding author: Tuo Fu.)*

I. INTRODUCTION

The term space situational awareness (SSA) refers to the activities including surveillance of detectable space objects, identification, and prediction of the locations of natural and manmade objects that are orbiting the Earth, and prediction of space events, possible collisions, and threats. Among all SSA-related techniques, determining the state vector (position and velocity) or orbit elements of a space object, which is referred to as orbit determination, is the basis for other applications. Since the first artificial satellite, namely, Sputnik I, was launched by the USSR in 1957, the number of resident space objects (RSOs) has steadily increased. By July 25, 2018, more than 17 000 space objects were in catalog, of which approximately 70% were space debris [1]. When the latest-generation space surveillance facilities come into full operation, there will be more than millions of observations per day [2], [3]. However, compared with the huge number of observable RSOs, the observation resources remain highly limited, the observations for each object are sparse by nature and the single observation time can be very short. The availability of an initial orbit determination technique that uses very short arc observations is of substantial importance for it can provide the information for data association and sensor scheduling. As a type of chief sensor for space surveillance, radar has all-time, all-weather observation capabilities and can provide precise radial measurements such as slant range and radial velocity. Therefore, developing the IOD method based on very short arc radar measurements is valuable.

The orbit determination problem has a long history and has been extensively studied. The first works on IOD methods were carried out by Gauss and Laplace approximately two centuries ago [4], with the goal of determining the orbits of natural celestial bodies such as comets, asteroids, and planets. With the emergence of general-purpose electronic computer techniques, many computer-based iterative orbit determination methods were developed, among which the double-r iteration technique by Escobal [5] and the approach by Gooding [6] are typical. These methods are designed for angles-only data and, therefore, are suitable for optical sensors such as astronomical telescopes. If the radial range and pointing angles of a target can be obtained simultaneously, methods such as Gibbs', Herrick-Gibbs', and Lambert's [5] can be adopted to yield an initial orbit.

In many cases, short-arc observations contain too limited information to yield a full or physically meaningful orbit, which is the crux of the too short arc (TSA) problem. Milani *et al.* developed a new orbit determination method for TSA optical observations of heliocentric asteroids [7], [8]. It used a four-dimensional (4-D) vector that included angle and angle rate data as an attributable. Then, the range and range rate were restricted to a specific zone, which was called the admissible region, by imposing some physical constraints. Subsequently, the admissible region was sampled to form virtual asteroids (VAs) and these VAs, along with the covariance matrices that corresponded to the attributables were propagated to a future time to perform

correlation between different TSA observations. Once two TSA observations were confirmed to belong to the same object, there were sufficiently many observations to determine its orbit. Tommei *et al.* [9] extended this method to Earth-orbiting objects and Fujimoto *et al.* [10] used this method to correlate multiple optical observations for Earth-orbiting objects in Poincaré orbit element space. However, the admissible region approach is designed for underdetermined problems, where the number of observations is less than six in a single TSA. Another possible solution to the TSA problem is to use multisite radar observations, which was reported in [11] and [12]; however, multisite radar systems are usually of great complexity and may require the target to be in a common view field. In addition, Ansalone *et al.* [13] developed a new method that uses the genetic algorithm for space-based sensors and subsequently Hinagawa *et al.* [14] extended this method to ground-based sensors. However, these methods require observations in the middle of the observation arc to construct a fitness function; thus, the whole observation arc cannot be reduced too far in length. DeMars *et al.* [15] presented a method that is based on the admissible region and multiple-hypothesis filtering techniques for short-arc initial orbit determination. The authors tested tracking methods using angles-only and angle and angle-rate observations and proved that including angle rate data can improve the tracking accuracy and accelerate the convergence. This clearly reveals that there is additional information in the angle rate data. Since Abatzoglou *et al.* have proved that high-accuracy radar measurements for radial velocity and acceleration can be obtained with an extended integration time in [16], it is reasonable to consider whether the higher order radar radial measurements (velocity, acceleration, and jerk) could be used for orbit determination.

In this paper, we propose a novel very short arc IOD method that is based on single-site radar measurements. This method uses slant range, azimuth, and elevation angles to determine the position vector and higher order radial measurements (velocity, acceleration, and jerk) to determine the velocity vector. Since the variances of higher order radial measurements decrease dramatically as the integration time increases, with approximately 10 s of coherent integration, radar can obtain sufficiently accurate radial measurements to support the IOD application. Thus, for a newly found LEO object, the continuous observation time can be reduced to about 10 s to extract its initial orbit parameters.

The remainder of this paper is organized as follows: Section II introduces the observation model and the IOD method, along with related coordinate systems under the spherical nonrotating Earth assumption. Then, the corrections for the Earth's rotation and oblateness are presented. Section III presents the linearized accuracy analysis that is based on the GDOP metric. Section IV focuses on the relations between the observation geometry and the GDOP. Then, the best observation geometry for the velocity dilution of precision (VDOP) is obtained under the near-circular constraint. Section V presents Monte Carlo simulations for a typical LEO satellite under two observation geometry configurations. Finally, Section VI draws the conclusion of this paper.

II. METHOD OF INITIAL ORBIT DETERMINATION

A. Observation Model

First, we introduce the coordinate systems that are used to describe the radar measurements. The Earth-centered coordinate systems, including the Earth-Centered Inertial (ECI) system and the Earth-Centered Fixed (ECF) system, are extensively used in SSA; their definitions can be found in [17].

The simplified transformation matrices between ECI and ECF are

$$\mathbf{M}_{\text{ECF}\leftarrow\text{ECI}} = \mathbf{R}_3\left(\theta_G\right) \tag{1a}$$

$$\mathbf{M}_{\text{ECI}\leftarrow\text{ECF}} = \mathbf{M}_{\text{ECF}\leftarrow\text{ECI}}^T \tag{1b}$$

where $\mathbf{R}_3\left(\cdot\right)$ denotes the rotation matrix around the Z-axis and θ_G is the Greenwich sidereal time. The effects of polar motion, nutation, and precession are neglected.

The radar measurements are described in the topocentric horizon system. Its origin is located at the observation point and the local horizon forms the fundamental plane. The X-axis points east from the site, the Y-axis points north, and the Z-axis is normal to the fundamental plane and directed toward the zenith. This implementation of the topocentric horizon system is denoted as ENZ while it may be rotated and used as SEZ in some other applications. The transformation matrices between the ECF and ENZ coordinate systems are

$$\mathbf{M}_{\text{ECF}\leftarrow\text{ENZ}} = \mathbf{R}_3\left(-90° - \lambda\right) \cdot \mathbf{R}_1\left(-90° + \phi\right) \tag{2a}$$

$$\mathbf{M}_{\text{ENZ}\leftarrow\text{ECF}} = \mathbf{M}_{\text{ECF}\leftarrow\text{ENZ}}^T \tag{2b}$$

where ϕ and λ denote the site geodetic latitude and longitude, respectively, and $\mathbf{R}_1\left(\cdot\right)$ is the rotation matrix around the X-axis. The definitions of three rotation matrices $\mathbf{R}_1(\cdot)$, $\mathbf{R}_2(\cdot)$, and $\mathbf{R}_3(\cdot)$ can be found in [18]. In this coordinate system, the azimuth, which is denoted as A, is measured from north, clockwise to the target position vector, and it has a value from $0°$ to $360°$. The elevation, which is denoted as E, is measured from the local horizon to the target position vector and it takes a value from $-90°$ to $90°$. If the value of E is negative, the target stays below the local horizon, which makes it invisible.

For simplicity, the Earth is modeled as an ideal sphere and the Earth's rotation is neglected initially. Under the above assumptions, the target motion is modeled as an unperturbed two-body problem. A ground-based radar produces six measurements, which are denoted as $\bar{\mathbf{Y}} = \left[\rho, A, E, \dot{\rho}, \ddot{\rho}, \dddot{\rho}\right]^T$, where ρ is the slant range, A and E are the pointing angles that are defined in the ENZ coordinate system, and $\dot{\rho}$, $\ddot{\rho}$, and $\dddot{\rho}$ are the target radial velocity, radial acceleration, and radial jerk, respectively.

The slant range ρ is the norm of relative position vector $\vec{r} - \vec{R}$:

$$\rho = \sqrt{\left(\vec{r} - \vec{R}\right)^2} \tag{3}$$

where $\vec{r}$ and $\vec{R}$ are the target position vector and the site position vector in ECI, respectively. Since the Earth is stationary, $\vec{R}$ is a constant vector.

The angle measurements are expressed as follows:

$$A = \arctan\left(\frac{\rho_E}{\rho_N}\right) \tag{4a}$$

$$E = \arctan\left(\frac{\rho_Z}{\sqrt{\rho_E^2 + \rho_N^2}}\right) \tag{4b}$$

where $\vec{\rho}_{\mathrm{ENZ}} = [\rho_E, \rho_N, \rho_Z]^T$ is the relative position vector in the ENZ system. Note that the value of A may need to be adjusted to fall in the range of $0°$–$360°$.

Differentiating ρ with respect to time yields

$$\dot{\rho} = \frac{\dot{\vec{r}} \cdot \left(\vec{r} - \vec{R}\right)}{\rho}. \tag{5}$$

Similarly, $\ddot{\rho}$ and $\dddot{\rho}$ can be expressed as follows:

$$\ddot{\rho} = \frac{\left(v^2 - \dot{\rho}^2\right) + \ddot{\vec{r}} \cdot \left(\vec{r} - \vec{R}\right)}{\rho} \tag{6}$$

$$\dddot{\rho} = -\frac{3\dot{\rho}\ddot{\rho}}{\rho} + \frac{3\dot{\vec{r}} \cdot \ddot{\vec{r}}}{\rho} + \frac{\dddot{\vec{r}} \cdot \left(\vec{r} - \vec{R}\right)}{\rho} \tag{7}$$

where $v = \left\|\dot{\vec{r}}\right\|$ is the norm of the velocity vector.

Since the target is driven by the Earth's central attraction only, the acceleration vector of the target can be expressed as

$$\ddot{\vec{r}} = -\frac{\mu_e}{r^3}\vec{r} \tag{8}$$

where μ_e is the Earth's gravitational constant and $r = \left\|\vec{r}\right\|$ is the target geocentric distance. Differentiating (8) with respect to time yields

$$\dddot{\vec{r}} = -\frac{\mu_e}{r^3}\dot{\vec{r}} + 3\mu_e\frac{\vec{r} \cdot \dot{\vec{r}}}{r^5}\vec{r}. \tag{9}$$

Substituting (8) and (9) into (6) and (7) yields the final expressions for the radial acceleration $\ddot{\rho}$ and the radial jerk $\dddot{\rho}$:

$$\ddot{\rho} = \frac{1}{\rho}\left(v^2 - \dot{\rho}^2\right) - \frac{\mu_e}{\rho r} + \frac{\mu_e}{\rho r^3}\left(\vec{r} \cdot \vec{R}\right) \tag{10}$$

$$\dddot{\rho} = -\frac{3\dot{\rho}\ddot{\rho}}{\rho} - \frac{\mu_e}{r^3}\dot{\rho} - \frac{3\mu_e\left(\vec{r} \cdot \vec{R}\right)}{\rho r^5}\left(\vec{r} \cdot \dot{\vec{r}}\right). \tag{11}$$

B. Determination of Position and Velocity

If the Earth is stationary, ECF becomes an inertial reference frame and the rotation angle θ_G between ECI and ECF is a constant. Given the slant range ρ and pointing angles
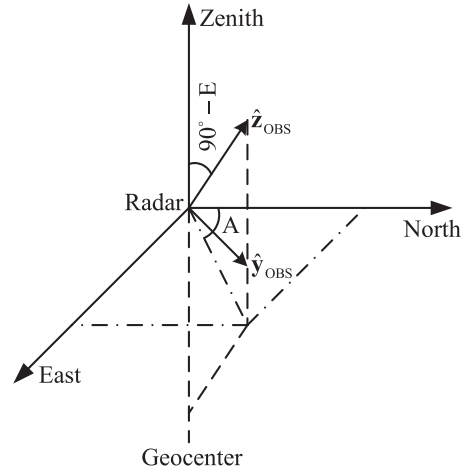

Fig. 1. Illustration of the ENZ and OBS coordinate systems.

A and E, the target position can be obtained directly via a series of coordinate transformations.

First, a transformation from spherical coordinates to Cartesian coordinates is performed to yield the relative position in the ENZ system:

$$\vec{\rho}_{\mathrm{ENZ}} = \begin{bmatrix} \rho\cos(E)\sin(A) \\ \rho\cos(E)\cos(A) \\ \rho\sin(E) \end{bmatrix}. \tag{12}$$

Then, the target position in ENZ is

$$\vec{r}_{\mathrm{ENZ}} = \vec{\rho}_{\mathrm{ENZ}} + \vec{R}_{\mathrm{ENZ}} \tag{13}$$

where $\vec{R}_{\mathrm{ENZ}}$ is the position vector of the ground radar site in ENZ.

Finally, the target position in ECI is

$$\vec{r}_{\mathrm{ECI}} = \mathbf{M}_{\mathrm{ECI\leftarrow ENZ}} \cdot \vec{r}_{\mathrm{ENZ}} \tag{14}$$

where $\mathbf{M}_{\mathrm{ECI\leftarrow ENZ}}$ is the transformation matrix from ENZ to ECI and it is expressed as

$$\mathbf{M}_{\mathrm{ECI\leftarrow ENZ}} = \mathbf{M}_{\mathrm{ECI\leftarrow ECF}} \cdot \mathbf{M}_{\mathrm{ECF\leftarrow ENZ}}. \tag{15}$$

To determine the velocity vector, at least three independent algebraic conditions are needed: the radial velocity $\dot{\rho}$ provides the projection of the target velocity vector on the radar line of sight (LOS); the radial acceleration $\ddot{\rho}$ constrains the norm of the velocity vector; and the radial jerk $\dddot{\rho}$ provides another projection of the velocity vector, namely, the projection on the direction of the target position vector. Therefore, the velocity vector $\dot{\vec{r}}$ can be determined using another three measurements: $\dot{\rho}$, $\ddot{\rho}$, and $\dddot{\rho}$.

Another useful orthogonal coordinate system for determining the velocity is the observation coordinate system, which is designated as OBS. As shown in Fig. 1, the origin coincides with the ENZ origin and the radar-geocenter-target plane forms the Y–Z plane. The Z-axis is directed from the site to the target, the X-axis is normal to the Y–Z plane and directed toward the right-hand side when it is viewed from the site toward the target, and the Y-axis is defined by the right-hand rule. Assuming the target has

an azimuth A and an elevation E, the transformation matrices between ENZ and OBS can be obtained via simple coordinate rotations as follows:

$$\mathbf{M}_{\text{OBS}\leftarrow\text{ENZ}} = \mathbf{R}_1\,(E - 90°) \cdot \mathbf{R}_3\,(-A) \tag{16a}$$

$$\mathbf{M}_{\text{ENZ}\leftarrow\text{OBS}} = \mathbf{M}_{\text{OBS}\leftarrow\text{ENZ}}^T. \tag{16b}$$

It is noted that both $\mathbf{M}_{\text{OBS}\leftarrow\text{ENZ}}$ and $\mathbf{M}_{\text{ENZ}\leftarrow\text{OBS}}$ are related to measurements. Therefore, they are both affected by measurement noise. If the target has a $90°$ elevation, the azimuth is undefined and this coordinate system is singular.

First, we solve for the target velocity vector in OBS. Then, a series of coordinate rotations are performed to obtain the velocity vector in ECI.

Let $\vec{\mathbf{v}}_{\text{OBS}} = \begin{bmatrix} v_x, v_y, v_z \end{bmatrix}^T$ denote the target velocity in OBS and $\vec{\mathbf{v}}_\perp$ denote the traverse (X–Y) component of $\vec{\mathbf{v}}_{\text{OBS}}$. According to the definition of the OBS coordinate system,

$$v_z = \dot{\rho}. \tag{17}$$

The equation for the norm of $\vec{\mathbf{v}}_\perp$ can be obtained directly from (10)

$$v_\perp^2 = v^2 - \dot{\rho}^2 = \rho\ddot{\rho} + \frac{\mu_e}{r} - \frac{\mu_e}{r^3}\vec{\mathbf{r}} \cdot \vec{\mathbf{R}} \tag{18}$$

where $v_\perp = \left\| \vec{\mathbf{v}}_\perp \right\|$.

For simplicity but without loss of generality, assuming that the radar site is located at the surface of the Earth, which means the altitude of the site is zero. Then, r and $\vec{\mathbf{r}} \cdot \vec{\mathbf{R}}$ satisfy

$$r = \sqrt{\rho^2 + R_e^2 + 2\rho R_e \sin(E)} \tag{19}$$

$$\vec{\mathbf{r}} \cdot \vec{\mathbf{R}} = R_e^2 + \rho R_e \sin(E). \tag{20}$$

From (11), we obtain

$$\vec{\mathbf{r}} \cdot \dot{\vec{\mathbf{r}}} = -\frac{\rho\dddot{\rho}r^5 + 3\dot{\rho}\ddot{\rho}r^5 + \mu_e\rho\dot{\rho}r^2}{3\mu_e\left(\vec{\mathbf{r}} \cdot \vec{\mathbf{R}}\right)}. \tag{21}$$

Since the position vector $\vec{\mathbf{r}}$ has already been determined, another expression for $\vec{\mathbf{r}} \cdot \dot{\vec{\mathbf{r}}}$ can be obtained:

$$\vec{\mathbf{r}} \cdot \dot{\vec{\mathbf{r}}} = -R_e \cos(E)v_y + (\rho + R_e \sin(E))\,\dot{\rho}. \tag{22}$$

Combining (21) and (22) yields

$$v_y = \frac{\rho\dddot{\rho}r^5 + 3\dot{\rho}\ddot{\rho}r^5 + \mu_e\rho\dot{\rho}r^2}{3\mu_e\left[R_e^2 + \rho R_e \sin(E)\right]R_e \cos(E)} + \frac{(\rho + R_e \sin(E))\,\dot{\rho}}{R_e \cos(E)}. \tag{23}$$

Finally,

$$v_x = \pm\sqrt{v_\perp^2 - v_y^2}. \tag{24}$$

Note that there are two ambiguous values for the velocity and additional information is needed to resolve the ambiguities. For instance, the angle change rates obtained from the radar servo system can be used to eliminate the ambiguities. If $E = 90°$, the denominator of (23) is zero, which is the singular case. Furthermore, if the site position vector lies in the orbital plane, which is referred to as

the coplanar case, v_x is always zero because the X-axis of the OBS coordinate system is perpendicular to the orbital plane. In this case, small measurement noise could lead to a complex-valued solution for the velocity vector. Therefore, we treat the whole visible arc in the coplanar case to be singular even if $E \neq 90°$. The above singular cases should be avoided when using the proposed method.

Once $\vec{\mathbf{v}}_{\text{OBS}}$ has been determined, the velocity in the ECI coordinate system can be obtained via rotations as follows:

$$\vec{\mathbf{v}}_{\text{ENZ}} = \mathbf{M}_{\text{ENZ}\leftarrow\text{OBS}} \cdot \vec{\mathbf{v}}_{\text{OBS}} \tag{25a}$$

$$\vec{\mathbf{v}}_{\text{ECI}} = \mathbf{M}_{\text{ECI}\leftarrow\text{ENZ}} \cdot \vec{\mathbf{v}}_{\text{ENZ}}. \tag{25b}$$

C. Corrections for the Earth′s Rotation and Oblateness

So far, the initial orbit determination method has been developed based on a nonrotating spherical Earth. However, the Earth's rotation and oblateness must be taken into consideration in practice. In this section, IOD corrections are made to account for the Earth's rotation and oblateness.

Due to the Earth's rotation, the site position vector $\vec{\mathbf{R}}$ becomes a time-dependent vector. Let $\vec{\mathbf{\Omega}}$ be the Earth's angular velocity vector. The site velocity, acceleration, and jerk vectors can be expressed as follows:

$$\dot{\vec{\mathbf{R}}} = \vec{\mathbf{\Omega}} \times \vec{\mathbf{R}} \tag{26a}$$

$$\ddot{\vec{\mathbf{R}}} = \vec{\mathbf{\Omega}} \times \dot{\vec{\mathbf{R}}} = \vec{\mathbf{\Omega}} \times \left(\vec{\mathbf{\Omega}} \times \vec{\mathbf{R}}\right) \tag{26b}$$

$$\dddot{\vec{\mathbf{R}}} = \vec{\mathbf{\Omega}} \times \ddot{\vec{\mathbf{R}}} = \vec{\mathbf{\Omega}} \times \left[\vec{\mathbf{\Omega}} \times \left(\vec{\mathbf{\Omega}} \times \vec{\mathbf{R}}\right)\right]. \tag{26c}$$

Then, the target radial range ρ, velocity $\dot{\rho}$, acceleration $\ddot{\rho}$, and jerk $\dddot{\rho}$ become

$$\rho = \sqrt{\left(\vec{\mathbf{r}} - \vec{\mathbf{R}}\right)^2} \tag{27}$$

$$\dot{\rho} = \frac{(\dot{\vec{\mathbf{r}}} - \dot{\vec{\mathbf{R}}}) \cdot \left(\vec{\mathbf{r}} - \vec{\mathbf{R}}\right)}{\rho} \tag{28}$$

$$\ddot{\rho} = \frac{\left[(\dot{\vec{\mathbf{r}}} - \dot{\vec{\mathbf{R}}})^2 - \dot{\rho}^2\right]}{\rho} + \frac{(\ddot{\vec{\mathbf{r}}} - \ddot{\vec{\mathbf{R}}}) \cdot \left(\vec{\mathbf{r}} - \vec{\mathbf{R}}\right)}{\rho} \tag{29}$$

$$\dddot{\rho} = -\frac{3\dot{\rho}\ddot{\rho}}{\rho} + \frac{3(\dot{\vec{\mathbf{r}}} - \dot{\vec{\mathbf{R}}}) \cdot (\ddot{\vec{\mathbf{r}}} - \ddot{\vec{\mathbf{R}}})}{\rho} + \frac{(\dddot{\vec{\mathbf{r}}} - \dddot{\vec{\mathbf{R}}}) \cdot \left(\vec{\mathbf{r}} - \vec{\mathbf{R}}\right)}{\rho}. \tag{30}$$

If we only consider the J_2 perturbation that is introduced by the Earth's oblateness, the target acceleration $\ddot{\vec{\mathbf{r}}}$ and jerk $\dddot{\vec{\mathbf{r}}}$ must be corrected as follows:

$$\ddot{\vec{\mathbf{r}}} = \ddot{\vec{\mathbf{r}}}_{2B} + \ddot{\vec{\mathbf{r}}}_{J_2} = -\frac{\mu_e}{r^3}\vec{\mathbf{r}} + \ddot{\vec{\mathbf{r}}}_{J_2} \tag{31}$$

$$\dddot{\vec{\mathbf{r}}} = \dddot{\vec{\mathbf{r}}}_{2B} + \dddot{\vec{\mathbf{r}}}_{J_2} = -\frac{\mu_e}{r^3}\dot{\vec{\mathbf{r}}} + 3\mu_e\frac{\vec{\mathbf{r}} \cdot \dot{\vec{\mathbf{r}}}}{r^5}\vec{\mathbf{r}} + \dddot{\vec{\mathbf{r}}}_{J_2} \tag{32}$$

where $\ddot{\vec{\mathbf{r}}}_{2B}$ and $\dddot{\vec{\mathbf{r}}}_{2B}$ are the two-body acceleration and jerk and $\ddot{\vec{\mathbf{r}}}_{J_2}$ and $\dddot{\vec{\mathbf{r}}}_{J_2}$ represent the J_2 perturbation acceleration and jerk, respectively. Concrete expressions for $\ddot{\vec{\mathbf{r}}}_{J_2}$ and $\dddot{\vec{\mathbf{r}}}_{J_2}$ are presented in Appendix A.

The target geocentric distance change rate $\dot{r}$ is expressed as

$$\frac{\dot{r}}{r} = \frac{\vec{\mathbf{r}} \cdot \dot{\vec{\mathbf{r}}}}{r^2}. \tag{33}$$

The Earth's rotation and oblateness do not affect the process of solving for the target position $\vec{\mathbf{r}}$. The key is to determine the target velocity $\dot{\vec{\mathbf{r}}}$. Suppose we know the site position vector $\vec{\mathbf{R}}$ accurately; then, $\dot{\vec{\mathbf{R}}}$, $\ddot{\vec{\mathbf{R}}}$, and $\dddot{\vec{\mathbf{R}}}$ could be determined immediately via (26). Once the target position $\vec{\mathbf{r}}$ has been obtained, $\dot{\vec{\mathbf{r}}}$ can also be determined via (31). Inspecting (28)–(30), we can conclude the following:

1) Equation (28) is a simple first-order equation for $\dot{x}$, $\dot{y}$, and $\dot{z}$.
2) The only unknown term in (29) is $(\dot{\vec{\mathbf{r}}} - \dot{\vec{\mathbf{R}}})^2$; thus, (29) is an second-order equation for $\dot{x}$, $\dot{y}$, and $\dot{z}$.
3) The unknown terms in (30) are $(\dot{\vec{\mathbf{r}}} - \dot{\vec{\mathbf{R}}})$ and $\dddot{\vec{\mathbf{r}}}$, both of which are first-order equations for $\dot{x}$, $\dot{y}$, and $\dot{z}$.

Theoretically, since (28)–(30) constitute three algebraic equations for $\dot{x}$, $\dot{y}$, and $\dot{z}$ for which the highest order is two, the solution for $\dot{\vec{\mathbf{r}}} = [\dot{x}, \ \dot{y}, \ \dot{z}]^T$ can be expressed analytically using all known quantities. However, the forms of these equations are highly complex; hence, a numerical method such as Newton–Raphson iteration is more advisable in practice. The initial velocity guess, which is denoted as $\dot{\vec{\mathbf{r}}}_{ini}$, can be obtained by following the steps that are described in Section II-B under the nonrotating Earth assumption.

III. ACCURACY ANALYSIS BASED ON GDOP

Since the analytical solution is only available for the nonrotating Earth, in this paper, we will only analyze the IOD accuracy under the nonrotating Earth assumption. Suppose that the radar has been elaborately calibrated and all system biases in the radar measurements have been removed. Thus, the measurements are corrupted by random noise only. The covariance matrix of the measurement noise is denoted as $\mathbf{C_Y}$.

Let $\vec{\mathbf{X}} = [\vec{\mathbf{r}}^T, \ \dot{\vec{\mathbf{r}}}^T]^T$ be the determined target state from the radar measurements in the ECI system, its covariance matrix is designated as $\mathbf{C_X}$. For linearized accuracy analysis, $\mathbf{C_X}$ is

$$\mathbf{C_X} = \frac{\partial \vec{\mathbf{X}}}{\partial \vec{\mathbf{Y}}^T} \cdot \mathbf{C_Y} \cdot \frac{\partial \vec{\mathbf{X}}^T}{\partial \vec{\mathbf{Y}}}. \tag{34}$$

The position dilution of precision (PDOP) and the velocity dilution of precision (VDOP) are defined as follows:

$$\text{PDOP} = \sqrt{\mathbf{C_X}(1, 1) + \mathbf{C_X}(2, 2) + \mathbf{C_X}(3, 3)} \tag{35a}$$

$$\text{VDOP} = \sqrt{\mathbf{C_X}(4, 4) + \mathbf{C_X}(5, 5) + \mathbf{C_X}(6, 6)}. \tag{35b}$$

A. Measurement Noise Model

Suppose a monopulse radar with the linear frequency modulation pulse train waveform is used to observe the target. Since the signal-to-noise ratio (SNR) for a single pulse

may be too low to perform a reliable detection, generally a period of time of signal integration is needed. The measurements are obtained at a reference time t_0. The target range ρ is derived directly from the time delay; the azimuth A and elevation E are acquired using the amplitude-comparison monopulse technique. The three higher order radial measurements $[\dot{\rho}, \ \ddot{\rho}, \ \dddot{\rho}]^T$ are estimated from the echo phases based on the target kinematic model. Because the measurements $[\rho, \ A, \ E]^T$ are irrelevant to the signal phase, $[\rho, \ A, \ E]^T$ and $[\dot{\rho}, \ \ddot{\rho}, \ \dddot{\rho}]^T$ are mutually independent. Thus, the covariance matrix can be partitioned as follows:

$$\mathbf{C_Y} = \begin{bmatrix} \mathbf{C}_{\rho AE} & \mathbf{0} \\ \mathbf{0} & \mathbf{C}_{\dot{\rho}\ddot{\rho}\dddot{\rho}} \end{bmatrix}. \tag{36}$$

The measurement noise for $[\rho, \ A, \ E]^T$ is modeled as a zero-mean Gaussian random vector with a diagonal covariance matrix $\text{diag}\{\sigma_\rho^2, \sigma_A^2, \sigma_E^2\}$. The standard deviation of ρ is typically several meters and the angle accuracy is typically one-tenth of the radar beam width for a monopulse radar [19].

The noise distribution for $[\dot{\rho}, \ \ddot{\rho}, \ \dddot{\rho}]^T$ is closely related to the target kinematic model and the estimation method. Suppose that a polynomial model is used to describe the radial motion of the target and the popular maximum-likelihood (ML) estimator is used to extract the coefficients of the polynomial model. One of the many good properties of the ML estimator is that it is asymptotically efficient [20], which means its output is unbiased, achieves the Cramér–Rao lower bound (CRLB) and has a Gaussian probability density function when the sample volume is very large. As a result, we model the measurement noise for $[\dot{\rho}, \ \ddot{\rho}, \ \dddot{\rho}]^T$ as a zero-mean Gaussian random vector with a covariance $\mathbf{C}_{\dot{\rho}\ddot{\rho}\dddot{\rho}}$ equals the inverse of the Fisher information matrix.

For a three-order polynomial target kinematic model, the CRLBs for the three higher order radial measurements are as follows [21]:

$$\sigma_{\dot{\rho}}^2 \geq \frac{75\lambda_0^2}{32\pi^2 T_D^2 \text{SNR}_{\text{int}}} \tag{37a}$$

$$\sigma_{\ddot{\rho}}^2 \geq \frac{45\lambda_0^2}{2\pi^2 T_D^4 \text{SNR}_{\text{int}}} \tag{37b}$$

$$\sigma_{\dddot{\rho}}^2 \geq \frac{3150\lambda_0^2}{\pi^2 T_D^6 \text{SNR}_{\text{int}}} \tag{37c}$$

where T_D is the integration time and SNR_{int} is the integrated SNR. λ_{RF}, λ_{RMS}, and λ_0 are expressed as follows:

$$\lambda_{\text{RF}} = \frac{c}{f_c} \tag{38a}$$

$$\lambda_{\text{RMS}} \approx \frac{c}{B/\sqrt{12}} \tag{38b}$$

$$\lambda_0 = \frac{\lambda_{\text{RF}}\lambda_{\text{RMS}}}{\sqrt{\lambda_{\text{RF}}^2 + \lambda_{\text{RMS}}^2}} \tag{38c}$$

where c is the light speed, f_c is the carrier frequency, and B is the signal bandwidth.

TABLE I
Radar System Parameters

Radar parameter	Value
Carrier frequency	3 GHz
Signal bandwidth	5 MHz
Integration time	10 s
Integrated SNR	25 dB
Radar beam width	1.2°

Table I shows the radar parameters used for the subsequent analysis and simulation.

If the reference time t_0 is chosen to be the exact middle point of the integration time interval, the covariance matrices $\mathbf{C}_{\rho A E}$ and $\mathbf{C}_{\dot\rho\ddot\rho\dddot\rho}$ corresponding to the parameters shown in Table I are as follows [21]:

$$\mathbf{C}_{\rho A E} = \begin{bmatrix} 0.4000\text{E}+1 & 0 & 0 \\ 0 & 0.1313\text{E}-1 & 0 \\ 0 & 0 & 0.1313\text{E}-1 \end{bmatrix} \quad (39a)$$

$$\mathbf{C}_{\dot\rho\ddot\rho\dddot\rho} = \begin{bmatrix} 0.7499\text{E}-7 & 0 & -0.2520\text{E}-7 \\ 0 & 0.0720\text{E}-7 & 0 \\ -0.2520\text{E-}7 & 0 & 0.1008\text{E}-7 \end{bmatrix} \quad (39b)$$

in which the units for angle, length, and time are degree, meter, and second, respectively. Note that only the two measurements $\dot\rho$ and $\dddot\rho$ are mutually correlated.

B. PDOP Analysis

Let $\vec{\mathbf{r}}_{\text{ENZ}}$ and $\mathbf{C}_{\text{ENZ}}^{\text{pos}}$ represent the determined position vector and its covariance matrix, respectively, in the ENZ system. Similarly, let $\vec{\mathbf{r}}_{\text{ECI}}$ and $\mathbf{C}_{\text{ECI}}^{\text{pos}}$ represent the corresponding vector and covariance matrix in ECI. Since $\vec{\mathbf{r}}_{\text{ENZ}}$ and $\vec{\mathbf{r}}_{\text{ECI}}$ are related by a linear transformation given by (14), the relation between $\mathbf{C}_{\text{ENZ}}^{\text{pos}}$ and $\mathbf{C}_{\text{ECI}}^{\text{pos}}$ should satisfy

$$\mathbf{C}_{\text{ECI}}^{\text{pos}} = \mathbf{M}_{\text{ECI}\leftarrow\text{ENZ}} \cdot \mathbf{C}_{\text{ENZ}}^{\text{pos}} \cdot \mathbf{M}_{\text{ECI}\leftarrow\text{ENZ}}^{T}. \quad (40)$$

Because the transformation matrix $\mathbf{M}_{\text{ECI}\leftarrow\text{ENZ}}$ is orthogonal, the traces of $\mathbf{C}_{\text{ENZ}}^{\text{pos}}$ and $\mathbf{C}_{ECF}^{\text{pos}}$ must be equal. Therefore, studying the PDOP in the ENZ system is sufficient.

In the ENZ system, the position vector is given by (12) and (13). Taking partial derivatives of $\vec{\mathbf{r}}_{\text{ENZ}}$ with respect to ρ, A, and E yield

$$\frac{\partial \vec{\mathbf{r}}_{\text{ENZ}}}{\partial \rho} = \frac{\partial \vec{\boldsymbol{\rho}}_{\text{ENZ}}}{\partial \rho} = \begin{bmatrix} \cos(E)\sin(A) \\ \cos(E)\cos(A) \\ \sin(E) \end{bmatrix} \quad (41a)$$

$$\frac{\partial \vec{\mathbf{r}}_{\text{ENZ}}}{\partial A} = \frac{\partial \vec{\boldsymbol{\rho}}_{\text{ENZ}}}{\partial A} = \begin{bmatrix} \rho\cos(E)\cos(A) \\ -\rho\cos(E)\sin(A) \\ 0 \end{bmatrix} \quad (41b)$$

$$\frac{\partial \vec{\mathbf{r}}_{\text{ENZ}}}{\partial E} = \frac{\partial \vec{\boldsymbol{\rho}}_{\text{ENZ}}}{\partial E} = \begin{bmatrix} -\rho\sin(E)\sin(A) \\ -\rho\sin(E)\cos(A) \\ \rho\cos(E) \end{bmatrix}. \quad (41c)$$

Then, the Jacobian matrix $\mathbf{J}_{\text{pos}}$ is expressed as

$$\mathbf{J}_{\text{pos}} = \begin{bmatrix} \dfrac{\partial \vec{\mathbf{r}}_{\text{ENZ}}}{\partial \rho}, & \dfrac{\partial \vec{\mathbf{r}}_{\text{ENZ}}}{\partial A}, & \dfrac{\partial \vec{\mathbf{r}}_{\text{ENZ}}}{\partial E} \end{bmatrix}. \quad (42)$$

The covariance matrix $\mathbf{C}_{\text{ENZ}}^{\text{pos}}$ is

$$\mathbf{C}_{\text{ENZ}}^{\text{pos}} = \mathbf{J}_{\text{pos}} \cdot \text{diag}\left\{\sigma_\rho^2,\ \sigma_A^2,\ \sigma_E^2\right\} \cdot \mathbf{J}_{\text{pos}}^{T}. \quad (43)$$

The PDOP is the square root of the trace of $\mathbf{C}_{\text{ENZ}}^{\text{pos}}$:

$$\text{PDOP} = \sqrt{\text{tr}\left(\mathbf{C}_{\text{ENZ}}^{\text{pos}}\right)} \quad (44)$$

where $\text{tr}(\cdot)$ is the trace operator.

Substituting (41)–(43) into (44) yields

$$\text{PDOP} = \sqrt{\sigma_\rho^2 + \rho^2\cos^2(E)\sigma_A^2 + \rho^2\sigma_E^2}. \quad (45)$$

Since the slant range standard deviation σ_ρ is small compared with the whole PDOP, a reasonable approximation of (45) is

$$\text{PDOP} \approx \sqrt{\rho^2\cos^2(E)\sigma_A^2 + \rho^2\sigma_E^2}. \quad (46)$$

Suppose the radar has the same angle accuracy in azimuth and elevation, namely, $\sigma_A^2 = \sigma_E^2 = \sigma_{\text{ANG}}^2$. Then, (46) can be further simplified to

$$\text{PDOP} \approx \sqrt{\rho^2\left[1 + \cos^2(E)\right]\sigma_{\text{ANG}}^2}. \quad (47)$$

Therefore, we conclude that in a single pass, if the orbit is an ideal circle, the highest accuracy for the position is always attained when the target is overhead because the target has minimum range ρ and maximum elevation E simultaneously.

C. VDOP Analysis

According to the process of velocity determination, we conclude that the determined velocity $\vec{\mathbf{v}}_{\text{ENZ}}$ is affected by all six measurements. Since $\vec{\mathbf{v}}_{\text{ENZ}}$ and $\vec{\mathbf{v}}_{\text{OBS}}$ are related via (25a), to obtain the Jacobian matrix $\partial\vec{\mathbf{v}}_{\text{ENZ}}/\partial\mathbf{Y}^T$, first the Jacobian Matrix $\partial\vec{\mathbf{v}}_{\text{OBS}}/\partial\mathbf{Y}^T$ is obtained and the concrete expression for each term in $\partial\vec{\mathbf{v}}_{\text{OBS}}/\partial\mathbf{Y}^T$ is presented in Appendix B. Due to the fact that the transformation matrix $\mathbf{M}_{\text{ENZ}\leftarrow\text{OBS}}$ is affected by the angle measurements, the partial derivatives of $\vec{\mathbf{v}}_{\text{ENZ}}$ are as follows:

$$\frac{\partial\vec{\mathbf{v}}_{\text{ENZ}}}{\partial\rho} = \mathbf{M}_{\text{ENZ}\leftarrow\text{OBS}} \cdot \frac{\partial\vec{\mathbf{v}}_{\text{OBS}}}{\partial\rho} \quad (48a)$$

$$\frac{\partial\vec{\mathbf{v}}_{\text{ENZ}}}{\partial A} = \frac{\partial\mathbf{M}_{\text{ENZ}\leftarrow\text{OBS}}}{\partial A} \cdot \vec{\mathbf{v}}_{\text{OBS}}$$
$$+ \mathbf{M}_{\text{ENZ}\leftarrow\text{OBS}} \cdot \frac{\partial\vec{\mathbf{v}}_{\text{OBS}}}{\partial A} \quad (48b)$$

$$\frac{\partial \vec{\mathbf{v}}_{\text{ENZ}}}{\partial E} = \frac{\partial \mathbf{M}_{\text{ENZ}\leftarrow\text{OBS}}}{\partial E} \cdot \vec{\mathbf{v}}_{\text{OBS}}$$

$$+ \mathbf{M}_{\text{ENZ}\leftarrow\text{OBS}} \cdot \frac{\partial \vec{\mathbf{v}}_{\text{OBS}}}{\partial E} \tag{48c}$$

$$\frac{\partial \vec{\mathbf{v}}_{\text{ENZ}}}{\partial \dot{\rho}} = \mathbf{M}_{\text{ENZ}\leftarrow\text{OBS}} \cdot \frac{\partial \vec{\mathbf{v}}_{\text{OBS}}}{\partial \dot{\rho}} \tag{48d}$$

$$\frac{\partial \vec{\mathbf{v}}_{\text{ENZ}}}{\partial \ddot{\rho}} = \mathbf{M}_{\text{ENZ}\leftarrow\text{OBS}} \cdot \frac{\partial \vec{\mathbf{v}}_{\text{OBS}}}{\partial \ddot{\rho}} \tag{48e}$$

$$\frac{\partial \vec{\mathbf{v}}_{\text{ENZ}}}{\partial \dddot{\rho}} = \mathbf{M}_{\text{ENZ}\leftarrow\text{OBS}} \cdot \frac{\partial \vec{\mathbf{v}}_{\text{OBS}}}{\partial \dddot{\rho}} \tag{48f}$$

where

$$\frac{\partial \mathbf{M}_{\text{ENZ}\leftarrow\text{OBS}}}{\partial A} =$$
$$\begin{bmatrix} -\sin(A) & \cos(A)\sin(E) & \cos(A)\cos(E) \\ -\cos(A) & -\sin(A)\sin(E) & -\sin(A)\cos(E) \\ 0 & 0 & 0 \end{bmatrix} \tag{49a}$$

$$\frac{\partial \mathbf{M}_{\text{ENZ}\leftarrow\text{OBS}}}{\partial E} =$$
$$\begin{bmatrix} 0 & \sin(A)\cos(E) & -\sin(A)\sin(E) \\ 0 & \cos(A)\cos(E) & -\cos(A)\sin(E) \\ 0 & \sin(E) & \cos(E) \end{bmatrix}. \tag{49b}$$

These two terms account for the error that is introduced by the coordinate transformation.

The Jacobian matrix $\mathbf{J}_{\text{vel}}$ is

$$\mathbf{J}_{\text{vel}} = \frac{\partial \vec{\mathbf{v}}_{\text{ENZ}}}{\partial \vec{\mathbf{Y}}^T}. \tag{50}$$

Then, the covariance matrix of $\vec{\mathbf{v}}_{\text{ENZ}}$ is

$$\mathbf{C}_{\text{ENZ}}^{\text{vel}} = \mathbf{J}_{\text{vel}} \cdot \mathbf{C}_{\mathbf{Y}} \cdot \mathbf{J}_{\text{vel}}^T. \tag{51}$$

Finally, the VDOP is the square root of the trace of $\mathbf{C}_{\text{ENZ}}^{\text{vel}}$:

$$\text{VDOP} = \sqrt{\text{tr}\left(\mathbf{C}_{\text{ENZ}}^{\text{vel}}\right)}. \tag{52}$$

D. Approximation of VDOP

Although (52) is rigorous, it lacks the necessary simplicity to support the observation geometry analysis. In this section, the approximation for VDOP is presented. Recall the process of velocity determination: we solve for the velocity in the OBS system, convert it to ENZ, and perform a series of rotations to obtain the velocity in ECI. Both the first step and the second step introduce errors, while the third step is error-free. The main strategy for approximation is to separate the VDOP into two parts: the error that is contained in $\vec{\mathbf{v}}_{\text{OBS}}$ and the error that is introduced by the coordinate transformation.

First, we consider the error that is contained in $\vec{\mathbf{v}}_{\text{OBS}} = [v_x, v_y, v_z]^T$. In this vector, v_z is just the radial velocity and its variance is small compared to the variances of other components. Therefore, only the error that is contained in
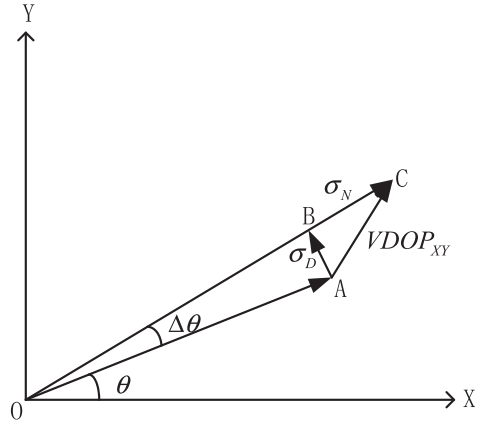

Fig. 2. VDOP in the X–Y plane of the OBS coordinate system.

the X–Y plane component, namely, $\vec{\mathbf{v}}_\perp = [v_x, v_y]^T$, needs to be considered.

As depicted in Fig. 2, in the X–Y plane, $\overrightarrow{OA}$ is the true velocity and $\overrightarrow{OC}$ is the determined velocity. The error vector $\overrightarrow{AC}$ is synthesized from the norm error $\overrightarrow{BC}$ and the direction error $\overrightarrow{AB}$. If the angle error $\Delta\theta$ is small, $\overrightarrow{AB}$ is approximately perpendicular to $\overrightarrow{BC}$. We can treat the three error vectors $\overrightarrow{AB}$, $\overrightarrow{BC}$, and $\overrightarrow{AC}$ as random variables and the norms of these vectors as their standard deviations. Since $\overrightarrow{AB}$ and $\overrightarrow{BC}$ are approximately orthogonal, the following relation can be established:

$$\text{VDOP}_{\text{XY}} \approx \sqrt{\sigma_N^2 + \sigma_D^2} \tag{53}$$

where VDOP_{XY} denotes the VDOP that corresponds to the X-Y components of the determined velocity and σ_N^2 and σ_D^2 denote the variances of the norm error and the direction error, respectively, for the X–Y components of determined velocity.

1) *Norm Error of $\vec{\mathbf{v}}_\perp$:* Monte Carlo simulation demonstrates that $v_\perp$ is mostly affected by the elevation angle noise. Taking the partial derivative of $v_\perp$ with respect to E yields

$$\frac{\partial v_\perp}{\partial E} = \frac{1}{2v_\perp} \frac{\partial v_\perp^2}{\partial E} \tag{54}$$

where $\partial v_\perp^2/\partial E$ is given by (84). Thus, the norm error is approximated as follows:

$$\sigma_N^2 \approx \left(\frac{\partial v_\perp}{\partial E}\right)^2 \sigma_E^2. \tag{55}$$

2) *Direction Error of $\vec{\mathbf{v}}_\perp$:* Let θ be the angle between $\vec{\mathbf{v}}_\perp$ and the positive direction of the OBS X-axis. It follows that

$$\theta = \arcsin\left(\frac{v_y}{v_\perp}\right). \tag{56}$$

Monte Carlo simulation demonstrates that θ is affected by the elevation and radial jerk noise significantly, while other measurement noise can be neglected. The partial

derivatives of θ with respect to E and $\dddot{\rho}$ are given by

$$\frac{\partial \theta}{\partial E} = \frac{1}{v_x}\left(\frac{\partial v_y}{\partial E} - \frac{v_y}{v_\perp}\frac{\partial v_\perp}{\partial E}\right) \quad (57)$$

$$\frac{\partial \theta}{\partial \dddot{\rho}} = \frac{1}{v_x}\left(\frac{\partial v_y}{\partial \dddot{\rho}} - \frac{v_y}{v_\perp}\frac{\partial v_\perp}{\partial \dddot{\rho}}\right) \approx \frac{1}{v_x}\frac{\partial v_y}{\partial \dddot{\rho}} \quad (58)$$

where all the involved partial derivatives are given in Appendix B.

The variance of θ is

$$\sigma_\theta^2 \approx \left(\frac{\partial \theta}{\partial E}\right)^2 \sigma_E^2 + \left(\frac{\partial \theta}{\partial \dddot{\rho}}\right)^2 \sigma_{\dddot{\rho}}^2. \quad (59)$$

The variance of the direction error is

$$\sigma_D^2 \approx v_\perp^2 \sigma_\theta^2. \quad (60)$$

The VDOP in the X–Y plane is the square root of the sum of σ_N^2 and σ_D^2:

$$\text{VDOP}_{\text{XY}} \approx \sqrt{\sigma_N^2 + \sigma_D^2}. \quad (61)$$

Finally, the VDOP in the OBS coordinate system is

$$\text{VDOP}_{\text{OBS}} = \sqrt{\text{VDOP}_{\text{XY}}^2 + \sigma_\rho^2} \approx \text{VDOP}_{\text{XY}}. \quad (62)$$

3) *Coordinate Transformation Error:* Let $\text{VDOP}_{\text{ENZ}\leftarrow\text{OBS}}$ be the coordinate transformation error. It satisfies

$$\text{VDOP}_{\text{ENZ}\leftarrow\text{OBS}}^2$$

$$= \vec{v}_{\text{OBS}}^T \cdot \left(\frac{\partial \mathbf{M}_{\text{ENZ}\leftarrow\text{OBS}}}{\partial A}\right)^T \cdot \left(\frac{\partial \mathbf{M}_{\text{ENZ}\leftarrow\text{OBS}}}{\partial A}\right) \cdot \vec{v}_{\text{OBS}} \cdot \sigma_A^2$$

$$+ 2\vec{v}_{\text{OBS}}^T \cdot \left(\frac{\partial \mathbf{M}_{\text{ENZ}\leftarrow\text{OBS}}}{\partial A}\right)^T \cdot (\mathbf{M}_{\text{ENZ}\leftarrow\text{OBS}}) \cdot \frac{\partial \vec{v}_{\text{OBS}}}{\partial A} \cdot \sigma_A^2$$

$$+ \vec{v}_{\text{OBS}}^T \cdot \left(\frac{\partial \mathbf{M}_{\text{ENZ}\leftarrow\text{OBS}}}{\partial E}\right)^T \cdot \left(\frac{\partial \mathbf{M}_{\text{ENZ}\leftarrow\text{OBS}}}{\partial E}\right) \cdot \vec{v}_{\text{OBS}} \cdot \sigma_E^2$$

$$+ 2\vec{v}_{\text{OBS}}^T \cdot \left(\frac{\partial \mathbf{M}_{\text{ENZ}\leftarrow\text{OBS}}}{\partial E}\right)^T \cdot (\mathbf{M}_{\text{ENZ}\leftarrow\text{OBS}}) \cdot \frac{\partial \vec{v}_{\text{OBS}}}{\partial E} \cdot \sigma_E^2. \quad (63)$$

Suppose $\sigma_A^2 = \sigma_E^2 = \sigma_{\text{ANG}}^2$. Substituting (16), (48), and (49) into (63) yields

$$\text{VDOP}_{\text{ENZ}\leftarrow\text{OBS}}^2 = \left\|\vec{v}_{\text{OBS}}\right\|^2 \sigma_{\text{ANG}}^2$$

$$+ \left[(v_z \cos(E) + v_y \sin(E))^2 - 2v_z \frac{\partial v_y}{\partial E}\right]\sigma_{\text{ANG}}^2. \quad (64)$$

For a target with a near-circular orbit, $v_y \approx 0$ and $v_z \approx 0$ when the target is overhead; hence, (64) can be further simplified to $\left\|\vec{v}_{\text{OBS}}\right\|^2 \sigma_{\text{ANG}}^2$ at that time.

Finally, the approximated VDOP is

$$\text{VDOP} \approx \sqrt{\text{VDOP}_{\text{OBS}}^2 + \text{VDOP}_{\text{ENZ}\leftarrow\text{OBS}}^2}. \quad (65)$$

IV. RELATIONS BETWEEN GDOP AND OBSERVATION GEOMETRY

The observation geometry is described in the orbit coordinate system, which is designated as OBT. As depicted in Fig. 3, the origin is located at the geocenter (O) and the
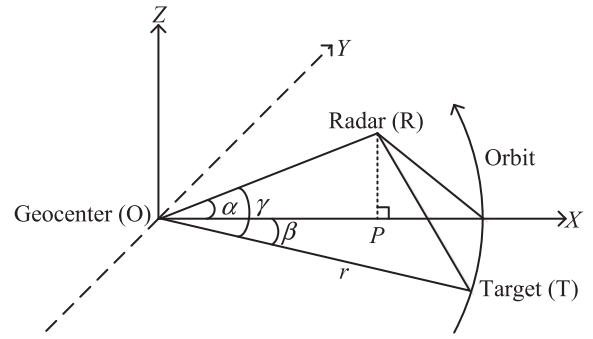

Fig. 3.   Illustration of the OBT coordinate system.

orbital plane forms the fundamental plane. The X-axis is extended through the projection point of the radar site (P), the Z-axis is normal to the orbital plane, and the Y-axis is determined by the right-hand rule. In this coordinate system, r is the geodistance of the target, α represents the angle between the site position vector, and the orbital plane and its value is between $-90°$ and $90°$, whereas β represents the angle between the target position vector and the X-axis and its value is between $-180°$ and $180°$. The angle between the radar site and the target is denoted by γ, which is fully determined by α and β, and it takes a value from $0°$ to $180°$. The three numbers, namely, $[r, \alpha, \beta]^T$, are referred to as observation geometry quantities. Both PDOP and VDOP are closely related to the observation geometry. Since most RSOs in low-Earth orbits have small eccentricities, in this part, the linkage between GDOP and the observation geometry is investigated under the near-circular constraint and the optimal observation geometry is identified. These analyses are all based upon a nonrotating Earth. The results could be used as a guide for the IOD epoch selection, for example.

Let i be the inclination and Ω be the right ascension of ascending node. Then, the angle α satisfies

$$\sin(\alpha) = \sin(\phi)\cos(i) + \cos(\phi)\sin(i)\sin(\Omega - \lambda - \theta_G). \quad (66)$$

If the Earth is stationary, α remains constant during a single pass.

A.   Condition of Small Eccentricity

When a target's orbit has sufficiently small eccentricity, it is reasonable to treat the visible arc as part of a circle in a single pass. In this section, we investigate the condition for conducting such an approximation.

As depicted in Fig. 4, O is the geocenter; P is the projection point of the radar site on the orbital plane; S is the intersection of the extension of OP and the target's elliptical orbit (the solid blue line), which is referred to as the collinear point; and f is the true anomaly of S. The solid black ellipse is the projection of the great circle containing the site and the dashed black line is the projection of the local horizon of the site. We approximate the visible arc (the portion above the dashed black line) as part of a
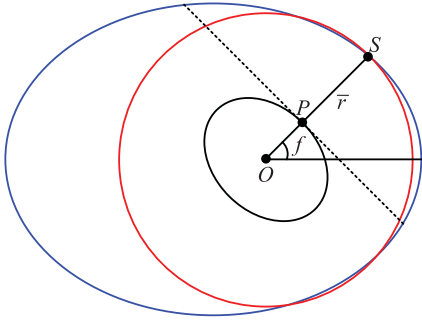
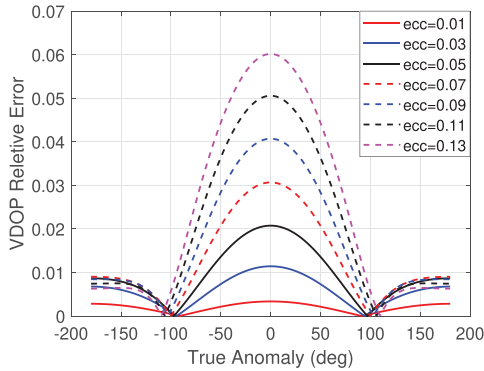Fig. 4.   Approximation of the visible arc with a circular arc.

Fig. 5.   VDOP relative error for the collinear point. The maximum relative error occurs at the perigee.
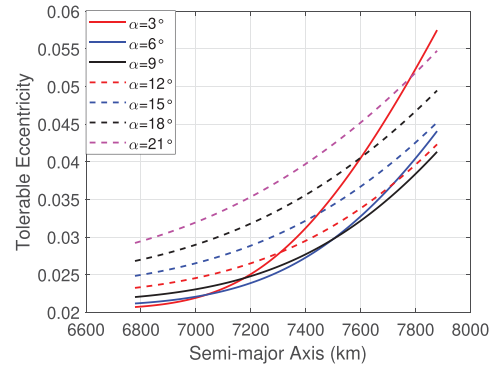

Fig. 6.   Tolerable eccentricity as a function of a and α.
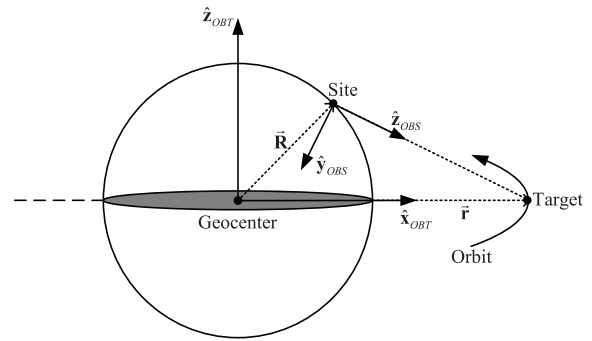
Fig. 7.   Illustration of the OBS and OBT coordinate systems.

circular orbit (the solid red line) with a radius $\bar{r}$, which is the geodistance of the collinear point.

For the approximated circular visible arc, both the PDOP and VDOP obtain their minimum values simultaneously at the collinear point S, which is justified by Figs. 8 and 9. If the eccentricity is small, we can expect that the minimum PDOP and VDOP for the true elliptical visible arc are obtained when the target is close to S. Thus, we pay special attention to the GDOP at the collinear point. Since the elliptical orbit and the approximated circular orbit are fully coincided at the collinear point, the PDOPs for both must be the same. However, the VDOP for the approximated circular orbit differs from the one for the original elliptical orbit at the collinear point.

Define ε_{clp} as the VDOP relative error between the circular arc and the elliptical arc at the collinear point

$$\varepsilon_{\text{clp}} = \frac{\left| \text{VDOP}_{\text{clp}}^{\text{cir}} - \text{VDOP}_{\text{clp}}^{\text{ell}} \right|}{\text{VDOP}_{\text{clp}}^{\text{ell}}} \tag{67}$$

where the subscript clp denotes the collinear point and the superscripts cir and ell indicate the circle and the ellipse, respectively.

The collinear point S could locate at any point of the whole orbit. Fig. 5 shows a typical group of curves of ε_{clp} versus the true anomaly and various eccentricities using the covariance matrix given by (36) and (39). Here, the semimajor axis a is chosen to be 7378 km and the site-orbital plane angle α is selected to be $8°$. We find that ε_{clp} attains its maximum value at the perigee. For a fixed

semimajor axis, ε_{clp} at the perigee tends to zero as the eccentricity tends to zero.

Let tol be a predefined threshold for ε_{clp}. For a fixed α angle, given a value of semimajor axis a, we can get the value of the eccentricity leading to $\varepsilon_{\text{clp}} = \text{tol}$ at the perigee. This eccentricity is referred to as the tolerable eccentricity, which means that any orbit with an eccentricity smaller than this one can be treated as a near-circular orbit given the corresponding (α, a) pair, and we can approximate any visible arc contained in this elliptical orbit using a circular arc described above.

Set tol $= 0.01$, for the measurement covariance matrix given by (36) and (39), the corresponding tolerable eccentricities versus the semimajor axes and the site-orbital plane angles are depicted in Fig. 6.

B.   GDOP for Near-Circular Orbits

Suppose that the target has a near-circular orbit, for the approximated circular visible arc, the target position and velocity vectors can be determined completely from the observation geometry quantities $[\bar{r}, \alpha, \beta]^T$ and only the angle β changes with time.

In the OBT coordinate system, the site position vector is expressed as

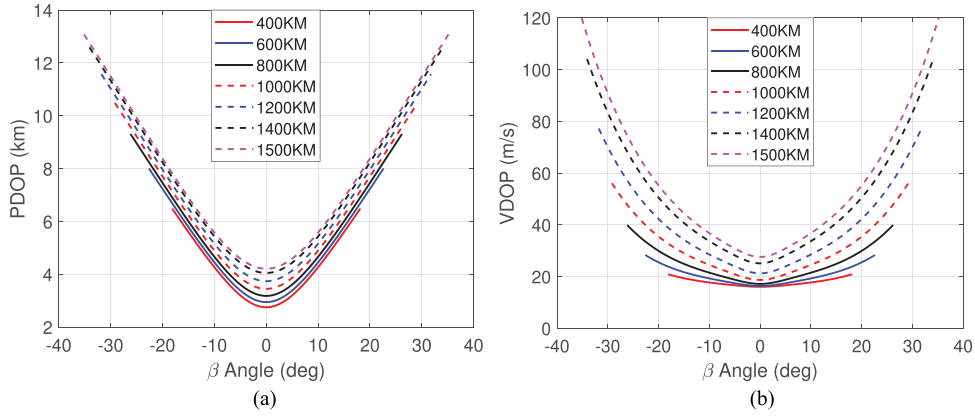$$\vec{\mathbf{R}} = \left[R_e \cos(\alpha), \ 0, \ R_e \sin(\alpha) \right]^T. \tag{68}$$

Fig. 8. GDOP versus orbit altitude. Both PDOP and VDOP are monotonically decreasing functions of the orbit altitude. (a) PDOP versus orbit altitude. (b) VDOP versus orbit altitude.
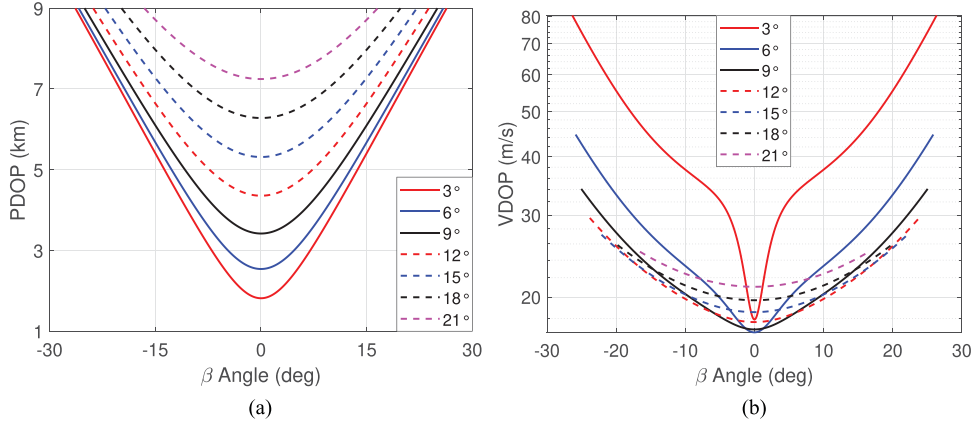

Fig. 9. GDOP versus site-orbital plane angle. Note that there is an optimal α angle that minimizes the VDOP. (a) PDOP versus site-orbital plane angle. (b) VDOP versus site-orbital plane angle.

The target position and velocity vectors are expressed as

$$\vec{\mathbf{r}} = \left[\bar{r}\cos(\beta), \ \bar{r}\sin(\beta), \ 0\right]^T \quad (69)$$

$$\vec{\mathbf{v}} \approx \left[-\sqrt{\mu_e/\bar{r}}\sin(\beta), \ \sqrt{\mu_e/\bar{r}}\cos(\beta), \ 0\right]^T. \quad (70)$$

The site-geocenter-target angle γ satisfies

$$\cos(\gamma) = \cos(\alpha)\cos(\beta). \quad (71)$$

By calculation, the elevation E satisfies

$$\sin(E) = \frac{\bar{r}}{\rho}\cos(\alpha)\cos(\beta) - \frac{R_e}{\rho} = \frac{\bar{r}}{\rho}\cos(\gamma) - \frac{R_e}{\rho} \quad (72a)$$

$$\cos(E) = \frac{\bar{r}}{\rho}\sqrt{1 - \cos^2(\alpha)\cos^2(\beta)} = \frac{\bar{r}}{\rho}\sin(\gamma). \quad (72b)$$

According to the cosine law, ρ satisfies

$$\rho = \sqrt{\bar{r}^2 + R_e^2 - 2\bar{r}R_e\cos(\gamma)}. \quad (73)$$

As shown in Fig. 7, the three axial unit vectors of the OBS system are

$$\hat{\mathbf{z}}_{\mathrm{OBS}} = \hat{\boldsymbol{\rho}} = \frac{\vec{\mathbf{r}} - \vec{\mathbf{R}}}{\left\|\vec{\mathbf{r}} - \vec{\mathbf{R}}\right\|} \quad (74a)$$

$$\hat{\mathbf{x}}_{\mathrm{OBS}} = \frac{\vec{\mathbf{r}} \times \vec{\mathbf{R}}}{\left\|\vec{\mathbf{r}} \times \vec{\mathbf{R}}\right\|} \quad (74b)$$

$$\hat{\mathbf{y}}_{\mathrm{OBS}} = \hat{\mathbf{z}}_{\mathrm{OBS}} \times \hat{\mathbf{x}}_{\mathrm{OBS}}. \quad (74c)$$

The three velocity components in the OBS system are

$$v_x = \vec{\mathbf{v}} \cdot \hat{\mathbf{x}}_{\mathrm{OBS}} \quad (75a)$$

$$v_y = \vec{\mathbf{v}} \cdot \hat{\mathbf{y}}_{\mathrm{OBS}} \quad (75b)$$

$$v_z = \vec{\mathbf{v}} \cdot \hat{\mathbf{z}}_{\mathrm{OBS}}. \quad (75c)$$

Using these relations, all of the six measurements can be expressed as functions of $[\bar{r}, \alpha, \beta]^T$ at any time except for the azimuth A, which is a free variable determined by a pair values of inclination i and right ascension of ascending node Ω. However, due to the symmetry of the spherical nonrotating Earth, any combination of i and Ω that satisfies (66) should be equivalent for evaluating the GDOP. Thus, the PDOP and VDOP can also be expressed

as functions of $[\bar{r}, \alpha, \beta]^T$. Since the final expressions are extremely complex, we will study their properties via their images later.

C. Effects of Observation Geometry on GDOP

Out of the three observation geometry quantities, $\bar{r}$ and α are free variables, while the range of values for β is constrained by the target visibility: given a pair $(\bar{r}, \alpha)$, the visible arc is determined under the restriction of $E > 0$ and different values of $(\bar{r}, \alpha)$ correspond to different visible arcs. Based upon this, in each run, we choose a typical value for either $\bar{r}$ or α and vary the value of the other to examine its influence on the GDOP. The measurement covariance matrix used in this section is given by (36) and (39).

1) *GDOP Versus $\bar{r}$:* The angle α is selected to be $8°$, which is a typical value for observing LEO targets. Assuming that the orbit eccentricity is zero and the orbit plane is aligned with the Earth's equatorial plane. The radar site is located at $(8°, 0°, 0\,\text{m})$. Due to the symmetry, such a configuration can be viewed as a representative of all the possible configurations. A series of values of orbit radius $\bar{r}$ are chosen to cover the entire LEO altitude (approximately 400 km–1500 km). For each value of the orbit radius, the visible arc is generated and the corresponding PDOP and VDOP are calculated based on our theory. The results are shown in Fig. 8.

From Fig. 8, we conclude that both PDOP and VDOP attain their minimum values when $\beta = 0°$, which is the overhead time. A larger orbital radius corresponds to a longer visible arc and both the minimum PDOP and VDOP increase with the orbital radius monotonically.

2) *GDOP Versus α:* A circular orbit is selected for testing. The orbit altitude is set to be 750 km and the orbit plane is aligned with the Earth's equatorial plane. A series of values of α are chosen to test the effects of them on the GDOP. Note that the exact zero value of α is excluded because this indicates the coplanar case and the VDOP is undefined according to (93), where the v_x term in the denominator equals zero. For each α angle, the latitude of the site is chosen to be equal to α and both the longitude and altitude of the site are assigned with zeros. Then, the visible arc for that virtual site is generated, and the PDOP and VDOP are calculated via our proposed method. The results are shown in Fig. 9.

As depicted in Fig. 9, the length of the visible arc increases as α decreases. For PDOP, the minimum value is attained when the target has maximum elevation. The minimum achievable PDOP decreases monotonically as α decreases. This is because a smaller value of α leads to a smaller minimum slant range $\rho_{\min}$ and a larger maximum elevation angle $E_{\max}$. According to (47), this corresponds to a smaller PDOP value. However, for VDOP, the rule becomes complex: although the minimum VDOP still occurs at the maximum elevation time in a single pass, the minimum achievable VDOP is no longer a monotonic function of α.

D. Optimal Observation Geometry for VDOP

From previous analysis, we conclude that there must be an optimal value of α that minimizes the VDOP and it should be related to both the orbit characteristics and the sensor measurement accuracy. Under the near-circular orbit condition, for a specified mean geocentric distance $\bar{r}$ and a radar measurement covariance matrix $\mathbf{C_Y}$, the optimal value of α can be determined uniquely. Suppose $\sigma_A^2 = \sigma_E^2 = \sigma_{\text{ANG}}^2$ and at the maximum elevation time, the following relations can be established:

$$v_x \approx \pm\sqrt{\mu_e/\bar{r}}, \quad v_y \approx 0, \quad v_z \approx 0, \quad v_\perp = |v_x| \approx \sqrt{\mu_e/\bar{r}}. \tag{76}$$

Substituting (76) into (54)–(55) yields the approximation for σ_N^2:

$$\frac{\partial v_\perp^2}{\partial E} \approx \frac{\mu_e R_e \left[3\cos(\alpha) R_e - 2\bar{r}\right]\sin(\alpha)}{\bar{r}^3} \tag{77a}$$

$$\sigma_N^2 \approx \frac{\mu_e R_e^2 [3\cos(\alpha) R_e - 2\bar{r}]^2 \sin^2(\alpha)}{4\bar{r}^5} \sigma_{\text{ANG}}^2. \tag{77b}$$

Substituting (76) into (57)–(60) yields the approximation for σ_D^2:

$$\frac{\partial \theta}{\partial E} \approx 0 \tag{78a}$$

$$\frac{\partial \theta}{\partial \dddot{\rho}} \approx \frac{\bar{r}^{7/2} \left[\bar{r}^2 - 2\bar{r}\cos(\alpha) R_e + R_e^2\right]}{3\mu_e^{3/2} R_e^2 \sin(\alpha)\cos(\alpha)} \tag{78b}$$

$$\sigma_D^2 \approx \frac{\bar{r}^6 \left[\bar{r}^2 - 2\bar{r}\cos(\alpha) R_e + R_e^2\right]^2}{9\mu_e^2 R_e^4 \sin^2(\alpha)\cos^2(\alpha)} \sigma_{\dddot{\rho}}^2. \tag{78c}$$

The minimum VDOP in a single pass is expressed as

$$\text{VDOP}_{\min} \approx \sqrt{\sigma_N^2 + \sigma_D^2 + \frac{\mu_e}{\bar{r}} \sigma_{\text{ANG}}^2}. \tag{79}$$

Then, the optimal value of α, which is denoted as α_{opt}, satisfies

$$\left.\frac{\partial \text{VDOP}_{\min}}{\partial \alpha}\right|_{\alpha=\alpha_{\text{opt}}} = 0. \tag{80}$$

However, (80) is too complex for its root to be determined analytically. Instead, the Newton iteration method can be used to find the root numerically. For the covariance matrix given by (36) and (39), the optimal value of α and its corresponding VDOP versus the orbit altitude are plotted in Fig. 10.

As can be seen in Fig. 10, the optimal value of α is symmetric about zero due to the symmetry of the observation geometry. The absolute value of α increases as the orbit altitude increases. The optimal value of α for an orbit altitude that corresponds to 750 km is approximately $6.25°$, which well agrees with Fig. 9(b).

V. SIMULATION RESULTS

A typical satellite of 750 km altitude in low Earth orbit is considered for the simulation purpose and the radar site is located at the Earth's equator. Monte Carlo experiments
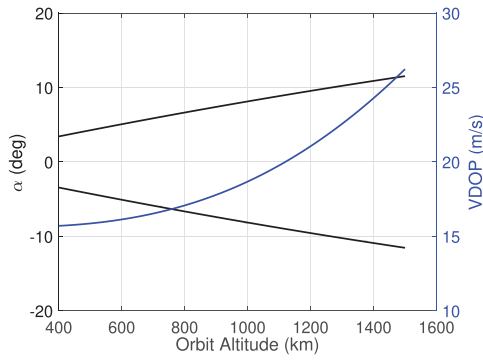
Fig. 10. Optimal site-orbital plane angle for the VDOP as a function of the orbit altitude.

TABLE II
Orbit Elements

Orbit parameter	Value
a	7129.332 km
e	0.0001492
i	98.4158°
Ω	68.4186°
ω	58.5638°

TABLE III
Geodetic Coordinates of Radar Sites

	Scenario 1	Scenario 2
Latitude	0°	0°
Longitude	-60°	35°
Altitude	0 km	0 km

with 100 000 runs are used to verify the validity of the proposed IOD method and the derived formulas for PDOP and VDOP. Two scenarios that correspond to two observation geometries are considered: one has a moderate maximum elevation angle of approximately 35°, while the other has a maximum elevation angle of approximately 65°, which is the nearly singular situation. In each scenario, a spherical nonrotating Earth is considered initially and the effects of the Earth's rotation and oblateness are subsequently examined. The radar parameters are shown in Table I and the measurement covariance matrix is given by (36) and (39). The orbital elements of the selected target are listed in Table II and the radar site coordinates are listed in Table III.

A. Nonsingular Case

In Fig. 11, the changes in the radar measurements over time are shown. We select the overhead time for the nonrotating Earth as the reference time. In each subplot, "NROT" is an abbreviation for the nonrotating Earth case and "ROT" is an abbreviation for the rotating Earth case. The target minimum slant range is approximately 1200 km and the maximum elevation angle is approximately 35°. Fig. 12 depicts the visible arc and the changes in the observation geometry over time. Due to the very small eccentricity (0.0001492), the target geocentric distance r varies less than 2 km over the whole visible arc. Therefore, assuming $\bar{r}$ is constant during a single pass is reasonable for the ob-
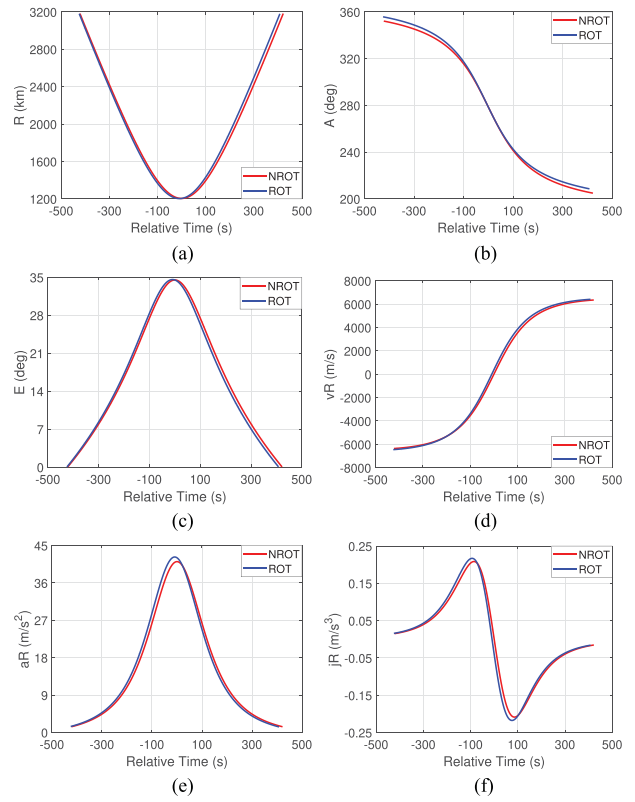

Fig. 11. Radar measurements for scenario 1. (a) Radial range. (b) Azimuth angle. (c) Elevation angle. (d) Radial velocity. (e) Radial acceleration. (f) Radial jerk.
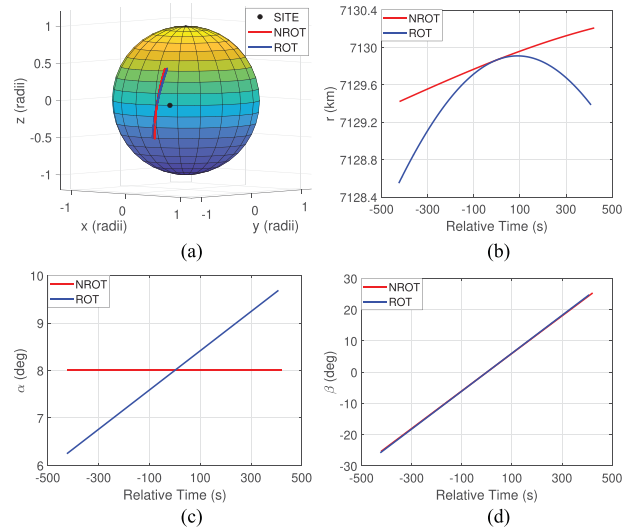

Fig. 12. Observation geometry for scenario 1. The α angle for the nonrotating Earth is about 8°, which is the nonsingular case. (a) Visible arc. (b) Geocentric distance. (c) α angle. (d) β angle.

servation geometry analysis. If the Earth is stationary, the site-orbital plane angle α remains unchanged.

Fig. 13 shows the approximation for the $\vec{v}_\perp$ error in the X–Y plane of the OBS system. In both subfigures, the legend "Full" means the error curve is obtained using all of the six noisy measurements. In Fig. 13(a), the legend "Part" means the error curve is obtained using the noisy elevation E only
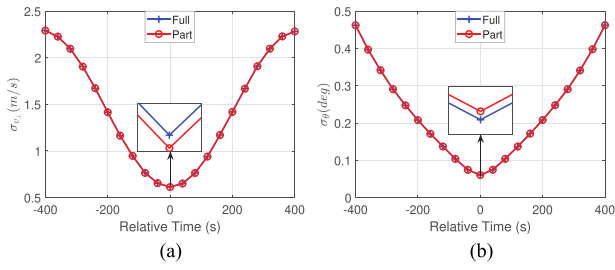
Fig. 13. Error approximation of $\vec{\mathbf{v}}_\perp$ for scenario 1. The accuracy of the approximation using partial noisy observations is high. (a) Norm error of $\vec{\mathbf{v}}_\perp$. (b) Direction error of $\vec{\mathbf{v}}_\perp$.
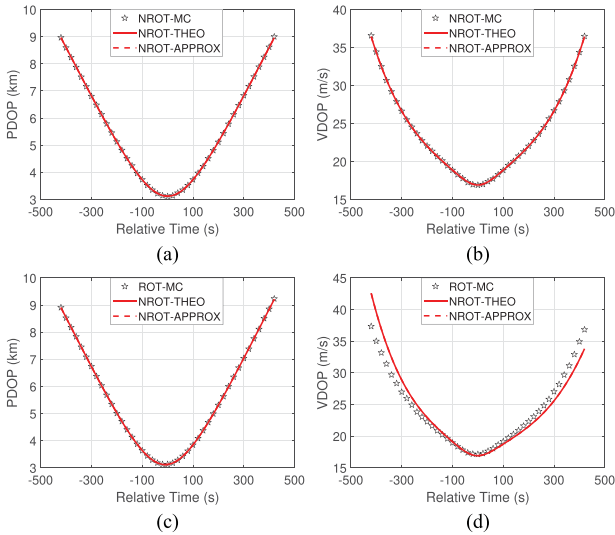

Fig. 14. Theoretical and simulated GDOP for scenario 1. (a) Nonrotating Earth PDOP. (b) Nonrotating Earth VDOP. (c) Rotating Earth PDOP. (d) Rotating Earth VDOP.
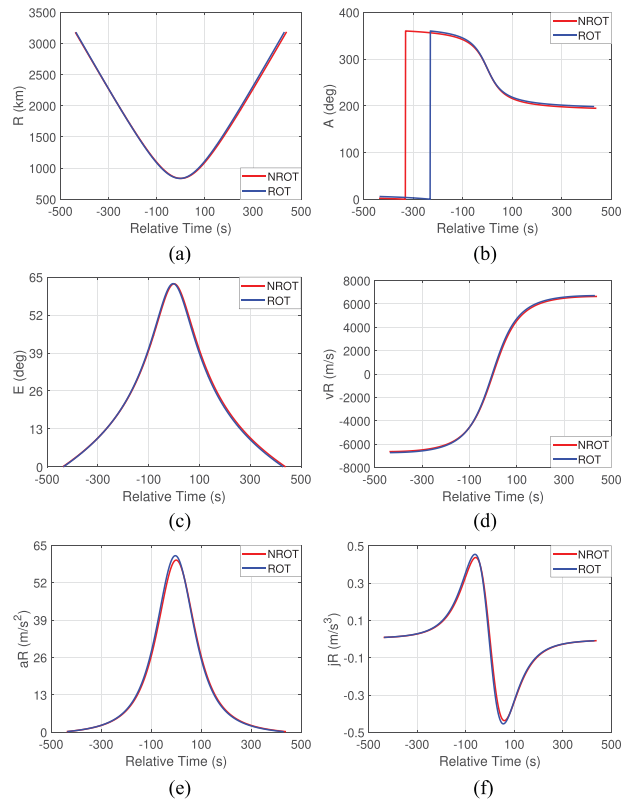

Fig. 15. Radar measurements for scenario 2. (a) Radial range. (b) Azimuth angle. (c) Elevation angle. (d) Radial velocity. (e) Radial acceleration. (f) Radial jerk.

while in Fig. 13(b), the legend "Part" means the curve is obtained using the noisy elevation E and radial jerk $\dddot{\rho}$. The results show that the approximation for the error contained in $\vec{\mathbf{v}}_\perp$ is accurate, which justifies the use of (55) and (59).

Fig. 14 depicts the theoretical GDOP and the simulated GDOP. The approximation accuracy is sufficiently high; hence, in all subplots, the solid line almost coincides with the dashed line. For the nonrotating Earth scenario, the consistency between the simulated GDOP and its theoretical counterpart demonstrates the validity of our derived formulas. The minimum values for PDOP and VDOP occur at the closest approach time or the maximum elevation time if the differences between these two times are neglected. The more the IOD epoch deviates from the overhead time, the lower the IOD accuracy will be. Hence, the lowest accuracy occurs when the target elevation angle is close to zero. In this scenario, the largest PDOP is approximately three times the smallest PDOP, while this number is approximately 2 for VDOP. For the rotating Earth scenario, the simulated PDOP well coincides with the theoretical PDOP because the Earth's rotation does not affect measurements ρ, A, and E. However, for the VDOP, there is a notable deviation between the theoretical value and the simulated value, especially when the target is just above the horizon. Since α

varies, the observation geometry is asymmetric. As a consequence, the theoretical VDOP becomes asymmetric. The error analysis for the rotating Earth scenario remains to be further investigated.

B. Near-Singular Case

In Scenario 2, the target has a maximum elevation angle of approximately $65°$, which corresponds to a site-orbital plane angle of approximately $3°$ for the stationary Earth. The radar measurements, the observation geometry, and the approximation for $\vec{\mathbf{v}}_\perp$ are depicted in Figs. 15–17, respectively. Since the site-orbital plane angle is close to zero, which is the singular case, the velocity accuracy should be lower than that in Scenario 1. Fig. 18 shows the theoretical GDOP and the simulated GDOP. As in Scenario 1, the optimal IOD epoch is the closest approach time/the maximum elevation time. The shape of the PDOP curve in Fig. 18(a) closely resembles the one in Fig. 14(a) except for a smaller minimum PDOP value due to a smaller minimum slant range. However, the VDOP curve differs from that in Scenario 1. As the time deviates from the reference time, the VDOP increases sharply and the largest VDOP is approximately 80 m/s, which is almost 5.5 times the smallest VDOP. This demonstrates the degradation in velocity accuracy when α is small. Like in Scenario 1, if the Earth's rotation is considered, the theoretical PDOP fits the simulated result well, while the theoretical VDOP is totally unreliable. However, the minimum VDOP value still
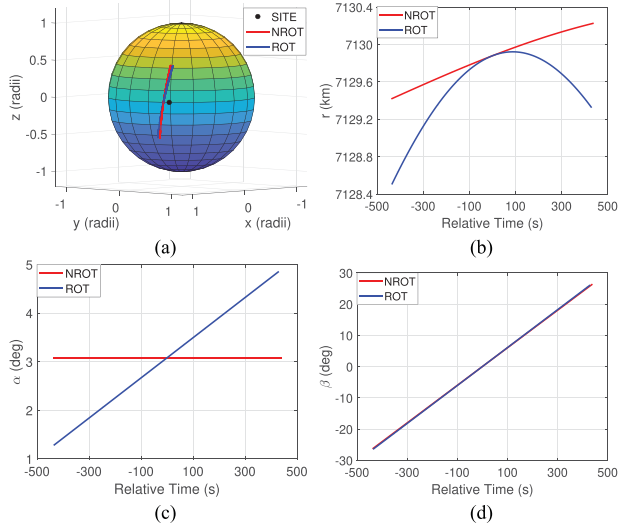
Fig. 16. Observation geometry for scenario 2. The α angle for the nonrotating Earth is about $3°$, which is the near-singular case. (a) Visible arc. (b) Geocentric Distance. (c) α angle. (d) β angle.
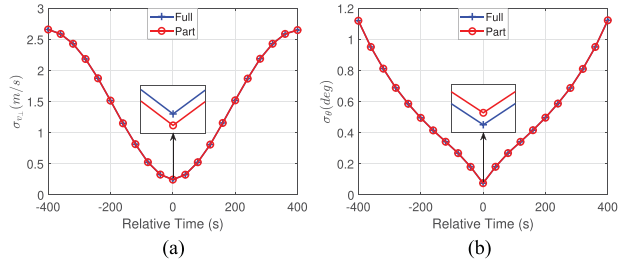

Fig. 17. Error approximation of $\vec{\mathbf{v}}_\perp$ for scenario 2. (a) Norm error of $\vec{\mathbf{v}}_\perp$. (b) Direction error of $\vec{\mathbf{v}}_\perp$.
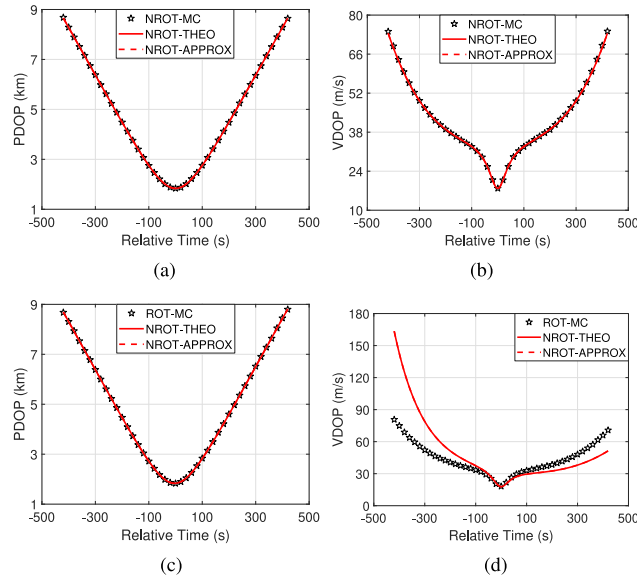

Fig. 18. Theoretical and Simulated GDOP for scenario 2. The deterioration of the VDOP is notable. (a) Nonrotating Earth PDOP. (b) Nonrotating Earth VDOP. (c) Rotating Earth PDOP. (d) Rotating Earth VDOP.

occurs around the maximum elevation time and our theoretical value well agrees with the simulated value at that time.

VI. CONCLUSION

In this paper, a new initial orbit determination method is proposed. The main feature of this method is that it uses high-accuracy radar radial measurements (velocity, acceleration, and jerk) to determine the target velocity vector. Linearized accuracy analysis is conducted and analytical expressions for PDOP and VDOP are derived. The relations between the above GDOP and the observation geometry are also investigated under the near-circular constraint. The results demonstrate that for objects that have near-circular orbits, the optimal observation time is always close to the maximum elevation time and there is an optimal angle between the site and orbital plane that minimizes the VDOP. These results could be used as a guide for observation arc selection. The method is verified with a typical LEO satellite via Monte Carlo experiments. The results demonstrate that for a typical integration time of approximately 10 s, the standard deviations for the determined position and velocity are several kilometers and several tens of meters per second, respectively.

Due to the fact that the CRLBs of radar radial measurements are reciprocal to the power of the integration time with an exponent that is greater than one, from a theoretical viewpoint, typically approximately 10 s of integration time is sufficient to yield a meaningful initial orbit, whereas the traditional IOD methods, such as Gauss', tend to yield unreasonable results under such a short time span. Because the high-accuracy radar radial measurements are derived from the phase information, this method can only be used for attitude-stable objects since a fast-changing attitude will destroy the phase relations between radar echoes.

APPENDIX A
J_2 PERTURBATION ACCELERATION AND JERK

$$\ddot{\mathbf{r}}_{J_2} = \frac{3}{2} J_2 \mu_e \frac{R_e^2}{r^4} \left[\frac{x}{r} \left(5\frac{z^2}{r^2} - 1 \right) \right] \hat{\mathbf{x}}$$
$$+ \frac{3}{2} J_2 \mu_e \frac{R_e^2}{r^4} \left[\frac{y}{r} \left(5\frac{z^2}{r^2} - 1 \right) \right] \hat{\mathbf{y}}$$
$$+ \frac{3}{2} J_2 \mu_e \frac{R_e^2}{r^4} \left[\frac{z}{r} \left(5\frac{z^2}{r^2} - 3 \right) \right] \hat{\mathbf{z}} \qquad (81)$$

$$\dddot{\mathbf{r}}_{J_2} = -5\frac{\dot{r}}{r}\ddot{\mathbf{r}}_{J_2}$$
$$+ \frac{3}{2} J_2 \mu_e \frac{R_e^2}{r^4} \left[\frac{\dot{x}}{r} \left(5\frac{z^2}{r^2} - 1 \right) + 10\frac{xz}{r^2} \left(\frac{\dot{z}}{r} - \frac{z}{r}\frac{\dot{r}}{r} \right) \right] \hat{\mathbf{x}}$$
$$+ \frac{3}{2} J_2 \mu_e \frac{R_e^2}{r^4} \left[\frac{\dot{y}}{r} \left(5\frac{z^2}{r^2} - 1 \right) + 10\frac{yz}{r^2} \left(\frac{\dot{z}}{r} - \frac{z}{r}\frac{\dot{r}}{r} \right) \right] \hat{\mathbf{y}}$$
$$+ \frac{3}{2} J_2 \mu_e \frac{R_e^2}{r^4} \left[\frac{\dot{z}}{r} \left(5\frac{z^2}{r^2} - 3 \right) + 10\frac{z^2}{r^2} \left(\frac{\dot{z}}{r} - \frac{z}{r}\frac{\dot{r}}{r} \right) \right] \hat{\mathbf{z}} \qquad (82)$$

where J_2 is the Earth's J_2 coefficient, μ_e is the Earth's gravitational constant, and R_e is the Earth's equatorial radius.

APPENDIX B
JACOBIAN MATRIX OF THE DETERMINED VELOCITY IN THE OBS SYSTEM

To obtain the Jacobian matrix, which is denoted as $\partial \vec{v}_{\text{OBS}}/\partial \mathbf{Y}^T$, the following partial derivatives are obtained step by step:

1) Partial derivatives of r

$$\frac{\partial r}{\partial \rho} = \frac{\rho + R_e \sin(E)}{r} \qquad \frac{\partial r}{\partial A} = 0$$
$$\frac{\partial r}{\partial E} = \frac{\rho R_e \cos(E)}{r} \qquad \frac{\partial r}{\partial \dot{\rho}} = 0$$
$$\frac{\partial r}{\partial \ddot{\rho}} = 0 \qquad \frac{\partial r}{\partial \dddot{\rho}} = 0. \tag{83}$$

2) Partial derivatives of $v_\perp^2$

$$\frac{\partial v_\perp^2}{\partial \rho} = \ddot{\rho} + \frac{\mu_e \left[R_e^3 \sin(E) - \rho^3 \right]}{r^5}$$
$$+ \frac{\mu_e \rho R_e^2 \left[3 + \cos(2E) - 2\sin(E) \right]}{2r^5}$$
$$\frac{\partial v_\perp^2}{\partial A} = 0$$
$$\frac{\partial v_\perp^2}{\partial E} = \frac{\mu_e \rho R_e \cos(E) \left[R_e^2 - 2\rho^2 - \rho R_e \sin(E) \right]}{r^5}$$
$$\frac{\partial v_\perp^2}{\partial \dot{\rho}} = 0 \qquad \frac{\partial v_\perp^2}{\partial \ddot{\rho}} = \rho \qquad \frac{\partial v_\perp^2}{\partial \dddot{\rho}} = 0. \tag{84}$$

3) Partial derivatives of v_z

$$\frac{\partial v_z}{\partial \rho} = 0 \qquad \frac{\partial v_z}{\partial A} = 0 \qquad \frac{\partial v_z}{\partial E} = 0$$
$$\frac{\partial v_z}{\partial \dot{\rho}} = 1 \qquad \frac{\partial v_z}{\partial \ddot{\rho}} = 0 \qquad \frac{\partial v_z}{\partial \dddot{\rho}} = 0. \tag{85}$$

4) Partial derivatives of v_y.
Let

$$N_1 = \rho \dddot{\rho} r^5 + 3\dot{\rho} \ddot{\rho} r^5 + \mu_e \rho \dot{\rho} r^2$$
$$D_1 = 3\mu_e \left[R_e^2 + \rho R_e \sin(E) \right] R_e \cos(E)$$
$$N_2 = (\rho + R_e \sin(E)) \dot{\rho}$$
$$D_2 = R_e \cos(E). \tag{86}$$

Then,

$$v_y = \frac{N_1}{D_1} + \frac{N_2}{D_2}. \tag{87}$$

Partial derivatives of N_1 are

$$\frac{\partial N_1}{\partial \rho} = \mu_e \dot{\rho} r^2 + \dddot{\rho} r^5 + (2\mu_e \rho \dot{\rho} + 5\rho \dddot{\rho} r^4$$
$$+ 15\dot{\rho} \ddot{\rho} r^4) \frac{\partial r}{\partial \rho}$$
$$\frac{\partial N_1}{\partial E} = \left(2\mu_e \rho \dot{\rho} r + 5\rho \dddot{\rho} r^4 + 15\dot{\rho} \ddot{\rho} r^4 \right) \frac{\partial r}{\partial E}$$
$$\frac{\partial N_1}{\partial A} = 0 \qquad \frac{\partial N_1}{\partial \dot{\rho}} = \mu_e \rho r^2 + 3\ddot{\rho} r^5$$
$$\frac{\partial N_1}{\partial \ddot{\rho}} = 3\dot{\rho} r^5 \quad \frac{\partial N_1}{\partial \dddot{\rho}} = \rho r^5. \tag{88}$$

Partial derivatives of D_1 are

$$\frac{\partial D_1}{\partial \rho} = 3\mu_e R_e^2 \sin(E) \cos(E) \quad \frac{\partial D_1}{\partial A} = 0$$
$$\frac{\partial D_1}{\partial E} = 3\mu_e R_e^2 \rho \cos(2E) \qquad \frac{\partial D_1}{\partial \dot{\rho}} = 0$$
$$\frac{\partial D_1}{\partial \ddot{\rho}} = 0 \qquad \frac{\partial D_1}{\partial \dddot{\rho}} = 0. \tag{89}$$

Partial derivatives of N_2 are

$$\frac{\partial N_2}{\partial \rho} = \dot{\rho} \qquad \frac{\partial N_2}{\partial A} = 0$$
$$\frac{\partial N_2}{\partial E} = R_e \dot{\rho} \cos(E) \quad \frac{\partial N_2}{\partial \dot{\rho}} = \rho + R_e \sin(E)$$
$$\frac{\partial N_2}{\partial \ddot{\rho}} = 0 \qquad \frac{\partial N_2}{\partial \dddot{\rho}} = 0. \tag{90}$$

Partial derivatives of D_2 are

$$\frac{\partial D_2}{\partial \rho} = 0 \quad \frac{\partial D_2}{\partial A} = 0 \quad \frac{\partial D_2}{\partial E} = -R_e \sin(E)$$
$$\frac{\partial D_2}{\partial \dot{\rho}} = 0 \quad \frac{\partial D_2}{\partial \ddot{\rho}} = 0 \quad \frac{\partial D_2}{\partial \dddot{\rho}} = 0. \tag{91}$$

Finally,

$$\frac{\partial v_y}{\partial Y_i} = \frac{1}{D_1} \frac{\partial N_1}{\partial Y_i} - \frac{N_1}{D_1^2} \frac{\partial D_1}{\partial Y_i}$$
$$+ \frac{1}{D_2} \frac{\partial N_2}{\partial Y_i} - \frac{N_2}{D_2^2} \frac{\partial D_2}{\partial Y_i} \tag{92}$$

where Y_i can be any of the six radar measurements.
5) Partial derivatives of v_x

$$\frac{\partial v_x}{\partial Y_i} = \frac{1}{2v_x} \frac{\partial v_\perp^2}{\partial Y_i} - \frac{v_y}{v_x} \frac{\partial v_y}{\partial Y_i}. \tag{93}$$

ACKNOWLEDGMENT

REFERENCES

[1] Space-Track.Org.
[Online]. Available: https://www.space-track.org/#boxscore

[2] H. Wilden, C. Kirchner, O. Peters, N. B. Bekhti, A. Brenner, and T. Eversberg
GESTRA–A phased-array based surveillance and tracking radar for space situational awareness
In *Proc. IEEE Int. Symp. Phased Array Syst. Technol.*, Waltham, MA, USA, 2016.

[3] D. L. Pechkis, N. S. Pacheco, and T. W. Botting
Statistical approach to the operational testing of space fence
IEEE Aerosp. Electron. Syst. Mag., vol. 31, no. 11, pp. 30–39, Nov. 2016.

[4] R. R. Karimi and D. Mortari
Initial orbit determination using multiple observations
Celestial Mech. Dynamical Astron., vol. 109, no. 2, pp. 167–180, 2011.

[5] P. R. Escobal
Methods of Orbit Determination. Hoboken, NJ, USA: Wiley, 1965.

[6] R. H. Gooding
A new procedure for the solution of the classical problem of minimal orbit determination from three lines of sight
Celestial Mech. Dynamical Astron., vol. 66, no. 4, pp. 387–423, 1997.

[7] A. Milani, G. F. Gronchi, M. de'Michieli Vitturi, and Z. Knežević
Orbit determination with very short arcs: I. Admissible regions
Celestial Mech. Dynamical Astron., vol. 90, no. 1/2, pp. 57–85, 2004.

[8] A. Milani, G. F. Gronchi, Z. Knežević, M. E. Sansaturio, and O. Arratia
Orbit determination with very short arcs: II. Identifications
Icarus, vol. 179, no. 2, pp. 350–374, 2005.

[9] G. Tommei, A. Milani, and A. Rossi
Orbit determination of space debris: Admissible regions
Celestial Mech. Dynamical Astron., vol. 97, no. 4, pp. 289–304, 2007.

[10] K. Fujimoto and D. J. Scheeres
Correlation of optical observations of earth-orbiting objects and initial orbit determination
J. Guid., Control, Dyn., vol. 35, no. 1, pp. 208–221, 2012.

[11] M. L. Smith
Tristatic tracking filter used by the multistatic measurement system
Lincoln Laboratory, MIT, Lexington, MA, USA, Tech. Rep. 699, 1984.

[12] H. Shang, D. Chen, H. Cao, T. Fu, and M. Gao
Initial orbit determination using very short arc data based on double-station observation
IEEE Trans. Aerosp. Electron. Syst., vol. 55, no. 4, pp. 1596–1611, Aug. 2019.

[13] L. Ansaloneand and F. Curti
A genetic algorithm for initial orbit determination from a too short arc optical observation
Adv. Space Res., vol. 52, no. 3, pp. 477–489, 2013.

[14] H. Hinagawa, H. Yamaoka, and T. Hanada
Orbit determination by genetic algorithm and application to geo observation
Adv. Space Res., vol. 53, no. 3, pp. 532–542, 2014.

[15] K. J. DeMars, M. K. Jah, and P. W. Schumacher, Jr.
Initial orbit determination using short-arc angle and angle rate data
IEEE Trans. Aerosp. Electron. Syst., vol. 48, no. 3, pp. 2628–2637, Jul. 2012.

[16] T. J. Abatzoglou and G. O. Gheen
Range, radial velocity, and acceleration MLE using radar LFM pulse train
IEEE Trans. Aerosp. Electron. Syst., vol. 34, no. 4, pp. 1070–1083, Oct. 1998.

[17] D. A. Vallado and W. D. McClain
Fundamentals of Astrodynamics and Applications, (ser. Space Technology Series). New York, NY, USA: McGraw-Hill, 1997, ch. 1, pp. 31–55.

[18] H. D. Curtis
Orbital Mechanics for Engineering Students. 3rd ed. Amsterdam, The Netherlands: Elseiver, 2014, ch. 4, pp. 202–216.

[19] G. R. Curry
Radar System Performance Modeling. 2nd ed. Norwood, MA, USA: Artech House, 2005, ch. 8, pp. 165–174.

[20] S. M. Kay
Fundamentals of Statistical Signal Processing: Estimation Theory (Prentice Hall Signal Processing Series). Englewood Cliffs, NJ, USA: Prentice-Hall, 1993, ch. 7, pp. 157–218.

[21] S. Ding, D. Chen, H. Cao, and T. Fu
Exact and closed-form CRLBS for high-order kinematic parameters estimation using LFM coherent pulse train
IEEE Access, vol. 6, pp. 57 447–57 459, 2018.
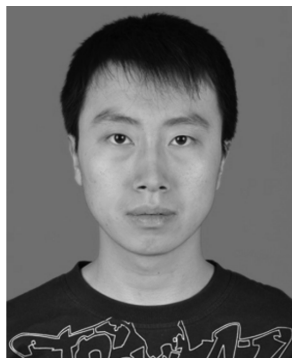
Shuo Zhang was born in Baoding, Hebei, China, in 1992. He received the B.S. degree in communication engineering from Beijing Institute of Technology, Beijing, China, in 2014, where he is currently working toward the Ph.D. degree in information and communication engineering.

His research interests include space situational awareness and statistical signal processing.

Tuo Fu was born in Shenyang, Liaoning, China, in 1977. He received the Ph.D. degree in electronic engineering from Beijing Institute of Technology, Beijing, China, in 2004.

From 2004 to 2006, he served as a Postdoctoral Researcher with the National Mobile Communications Research Laboratory, Southeast University, China. Since 2006, he has been an Associate Professor with the School of Information and Electronics, Beijing Institute of Technology. His research interests include radar system analysis and statistical signal processing.

Defeng Chen was born in Longyan, Fujian Province, China, in 1983. He received the B.S. and Ph.D. degrees in electronic engineering from Beijing Institute of Technology, Beijing, China, in 2006 and 2011, respectively.

He is currently a Lecturer with the School of Information and Electronics, Beijing Institute of Technology. His research interests include radar signal processing and its applications in space target detection.

Shuai Ding received the B.S. degree in electronic information science and technology from the College of Science, Xidian University, Xi'an, China, in 2010. He is currently working toward the Ph.D. degree in information and communication engineering at Beijing Institute of Technology, Beijing, China.

His research interests include radar system analysis, space debris surveillance, signal detection, and parameter estimation techniques.

Meiguo Gao received the B.S. and Ph.D. degrees in electronic engineering from Beijing Institute of Technology, Beijing, China, in 1988 and 1993, respectively.

From 2002 to 2003, he was a Senior Visiting Scholar at the University of Calgary, Canada. He is currently a Full Professor with the School of Information and Electronics, Beijing Institute of Technology. His primary research interests include real-time signal processing and radar system design.